

# Ocean Heat Convergence and North Atlantic Multidecadal Heat Content Variability

B. I. MOAT<sup>1</sup>,<sup>a</sup> B. SINHA,<sup>a</sup> DAVID I. BERRY,<sup>a</sup> S. S. DRIJFHOUT,<sup>b,c,d</sup> N. FRASER,<sup>e</sup> L. HERMANSON,<sup>f</sup> D. C. JONES,<sup>g</sup> S. A. JOSEY,<sup>a</sup> B. KING,<sup>a</sup> C. MACINTOSH,<sup>h</sup> A. MEGANN,<sup>a</sup> M. OLTMANN,<sup>a</sup> R. SANDERS,<sup>i</sup> AND S. WILLIAMS<sup>a</sup>

<sup>a</sup> National Oceanography Centre, Southampton, United Kingdom

<sup>b</sup> Royal Netherlands Meteorological Institute (KNMI), De Bilt, Netherlands

<sup>c</sup> Ocean and Earth Science, University of Southampton, Southampton, United Kingdom

<sup>d</sup> Faculty of Science, Utrecht University, Utrecht, Netherlands

<sup>e</sup> Scottish Association for Marine Science, Scotland, United Kingdom

<sup>f</sup> Met Office, Exeter, United Kingdom

<sup>g</sup> University of Michigan, Ann Arbor, Michigan

<sup>h</sup> ESA Climate Office, Harwell, Oxfordshire, United Kingdom

<sup>i</sup> NORCE, Norwegian Research Centre and Bjerknes Centre for Climate Research, Bergen, Norway

(Manuscript received 23 June 2023, in final form 3 May 2024, accepted 15 May 2024)

**ABSTRACT:** We construct an upper ocean (0–1000 m) North Atlantic heat budget (26°–67°N) for the period 1950–2020 using multiple observational datasets and an eddy-permitting global ocean model. On multidecadal time scales, ocean heat transport convergence controls ocean heat content (OHC) tendency in most regions of the North Atlantic with little role for diffusive processes. In the subpolar North Atlantic (45°–67°N), heat transport convergence is explained by geostrophic currents, whereas ageostrophic currents make a significant contribution in the subtropics (26°–45°N). The geostrophic contribution in all regions is dominated by anomalous advection across the time-mean temperature gradient although other processes make a significant contribution, particularly in the subtropics. The time scale and spatial distribution of the anomalous geostrophic currents are consistent with a simple model of basin-scale thermal Rossby waves propagating westward/northwestward in the subpolar gyre, and multidecadal variations in regional OHC are explained by geostrophic currents periodically coming into alignment with the mean temperature gradient as the Rossby wave passes through. The global ocean model simulation shows that multidecadal variations in the Atlantic meridional overturning circulation are synchronized with the ocean heat transport convergence consistent with modulation of the west–east pressure gradient by the propagating Rossby wave.

**SIGNIFICANCE STATEMENT:** The purpose of the work is to understand why the North Atlantic Ocean warms up and cools down on time scales of about 40 years. The key finding is that the temperature fluctuations are caused by an oceanic wave pushing the ocean surface up and down and causing ocean currents to change direction, pushing heat into and out of different parts of the ocean, and drawing down or emitting heat to the atmosphere. The findings matter because the warm and cool periods affect the climate of the countries surrounding the North Atlantic. Climate models need to account for this oceanic wave process to correctly predict how it will change in the future and affect the large-scale climate in a warming world.


**KEYWORDS:** North Atlantic Ocean; Meridional overturning circulation; Ocean circulation; Ocean dynamics; Rossby waves

## 1. Introduction

There is currently an increasing interest in decadal climate prediction. The World Climate Research Programme (WCRP) has designated Near-Term Climate Prediction as one of its Grand Challenges and decadal prediction features prominently in its Lighthouse Activity on Explaining and Predicting Earth System Change (WCRP 2023a,b). One of the areas of the globe with large potential decadal predictability is the North Atlantic (Yeager and Robson 2017) and clear decadal to multidecadal signals in multiple climate variables are seen there (Robson et al. 2018). Due to its long historical record, spatiotemporal coverage, and resolution, sea surface temperature (SST) is the defining variable for Atlantic multidecadal variability (AMV; Kushnir

1994). Skillful decadal prediction of any one of a number of related climate variables, for example, the North Atlantic Oscillation (NAO) index, the Atlantic meridional overturning circulation (AMOC), or North Atlantic Ocean heat content (OHC), would allow us to forecast climatic impacts of AMV (e.g., Enfield et al. 2001; Knight et al. 2006; Msadek and Frankignoul 2009; Sutton and Dong 2012; Sutton et al. 2018) in the adjacent countries in Europe, Africa, and North America and would bring significant socioeconomic benefits.

To confidently predict AMV a decade or more ahead, we need to understand the mechanism behind its decadal variability. Many modeling studies have proposed that the proximate driver of AMV is the AMOC [Robson et al. (2012); Zhang

 Denotes content that is immediately available upon publication as open access.

Corresponding author: Bengamin Moat, bim@noc.ac.uk

*Publisher's Note:* This article was revised on 24 February 2025 to update the copyright holder as the author(s).

*Publisher's Note:* This article was revised on 26 September 2024 to correct the affiliation of coauthor Berry, which was incorrect when originally published.

DOI: 10.1175/JCLI-D-23-0370.1

© 2024 Author(s). This published article is licensed under the terms of a Creative Commons Attribution 4.0 International (CC BY 4.0) License



(2008); Zhang and Zhang (2015), and see Zhang et al. (2019) for a comprehensive review of the subject], and there is also some evidence of this from proxy observations (McCarthy et al. 2015). The AMOC in turn is proposed to be driven by the NAO through its impact on oceanic deep convection (Robson et al. 2016). The AMV has also been proposed to feedback on the NAO via its subpolar SST signature raising the possibility of a coupled multidecadal oscillation (e.g., Sutton et al. 2018). However, other explanations of the AMV have been proposed. One suggests that the multidecadal oscillation is imposed on the ocean by atmospheric variability [Clement et al. (2015), but see Zhang et al. (2019) for a critique of this hypothesis], while another suggests that linked variability in both AMOC and AMV emerges as a result of an internal ocean mode of variability involving basin-scale “thermal” Rossby wave propagation across the subpolar gyre (Sévellec and Fedorov 2013, 2015).

Volcanoes (Otterå et al. 2010; Swingedouw et al. 2015) and anthropogenic aerosols (Booth et al. 2012) have been suggested to drive AMV. Robson et al. (2022) show that aerosols can impact the AMOC by modifying turbulent heat loss (and hence deep convection) over the subpolar gyre—a consequence of changing air temperatures over the North American continent. However, it is also possible that a specific external driver is not necessary as an existing mode of variability, either coupled, ocean-only, or atmospheric could be excited by a nonspecific injection of energy such as atmospheric weather noise (Sévellec and Huck 2015).

Another challenge has been the lack of agreement between models on the AMV characteristics and its mechanism (Drews and Greatbatch 2017; Muir and Fedorov 2017; Sévellec and Sinha 2018; Sutton et al. 2018). Even simulations with the same model but different resolutions may give different results. For example, a recent study (Lai et al. 2022) finds that density anomalies generated in the Labrador Sea are the dominant influence on the ocean circulation variability associated with AMV at eddy-permitting ocean resolution, but when a non-eddy-permitting resolution is used, density anomalies generated in the Nordic seas are more important.

Many authors have sought to understand the dynamic and thermodynamic drivers of subpolar SST using state estimates or observations (e.g., Buckley et al. 2014; Roberts et al. 2017; Josey and Sinha 2022). Although some progress has been made, this is complicated because the SST is related to the temperature of the surface mixed layer which varies in depth and whose heat budget is strongly influenced by entrainment. Some authors have compromised by taking the heat budget over a fixed climatological mixed layer depth at each location rather than the actual mixed layer depth (Buckley et al. 2014; Roberts et al. 2017) which reduces the link with the SST; others have compromised by using the actual mixed layer depth but at the cost of using a simplified heat budget (Josey and Sinha 2022). Additionally, surface heat fluxes and ocean heat transport convergence are more finely balanced than for the heat content over a larger fixed depth; hence, very accurate data are needed to attribute the dominant process (Moat et al. 2019). Dynamical attribution to the large-scale ocean circulation, the AMOC, for example, is also difficult as the ocean circulation typically extends over depth scales many times larger than typical mixed layer depths.

Here, our approach is to investigate the upper-ocean heat content, as this is an integral part of AMV. While there have been many studies investigating the link between AMOC and AMV (e.g., Robson et al. 2012; Zhang 2008; Zhang and Zhang 2015), these and others have focused on the link between the AMOC and the full-depth meridional ocean heat transport. These valuable studies are therefore limited in what they say about how changes in the full-depth meridional heat transport lead to changes in regional upper-ocean heat content.

In particular, the processes leading to regional heat transport convergence have received little attention even though for the purposes of skillful prediction it is necessary to faithfully reproduce the regional and temporal variation of the ocean heat transport convergence. These processes are the focus of the present study. As organized changes of OHC over large areas are needed to affect the overlying atmospheric circulation (the jet stream and the storm track), we focus on the North Atlantic Ocean heat budget over large spatial scales (1000+ km). We also choose a depth horizon of 1000 m (Buckley and Marshall 2016; Hirschi et al. 2020; Moat et al. 2019).

We address the following questions:

- 1) What is the relative importance of ocean versus atmosphere processes in driving upper-ocean heat content variability on multidecadal time scales?
- 2) Are changes in velocity, changes in a temperature gradient, or both important in determining the heat transport convergence, and what controls these changes?
- 3) How does ocean heat transport convergence relate to the AMOC?

The paper is organized as follows. In section 2, we describe data sources, ocean ice model setup, and our ocean heat budget decomposition. In section 3, we present our results, and section 4 concludes with a summary and discussion.

## 2. Data and methods

### a. Datasets

OHC was derived from gridded temperature–salinity datasets: EN4.2.2 (Good et al. 2013), Met Office Statistical Ocean Reanalysis (MOSORA) (Smith and Murphy 2007; Smith et al. 2015), and NOC Argo OI (Moat et al. 2021). SST and air–sea fluxes are obtained from the widely used ERA5 reanalysis (Hersbach et al. 2020). The OHC was estimated as the product of the volume, potential temperature, density ( $1000 \text{ kg m}^{-3}$ ), and specific heat capacity ( $4200 \text{ J kg}^{-1} \text{ K}^{-1}$ ). The dataset resolutions are detailed in Table 1. Absolute surface geostrophic currents based on satellite altimetry were obtained from the Copernicus Climate Change Service, Climate Data Store (2018). The vDT2021 data product used was used.

We use the NEMO ocean general circulation model (Madec et al. 2016) coupled with the CICE sea ice model (Hunke and Dukowicz 1997) in the global ocean 6 (GO6) configuration (Storkey et al. 2018), which has a nominal resolution of  $\sim 0.25^\circ$  and 75 vertical levels, to estimate the importance of ageostrophic

TABLE 1. The gridded temperature–salinity datasets.

	Spatial resolution	Vertical resolution	Temporal resolution
EN4.2.2	1° × 1°	42 levels	Monthly
MOSORA	1.25° × 1.25°	20 levels	Monthly
ArgoOI (surface to 2000 m)	1° × 1°	100 levels	10-day resolution averaged to monthly

effects. The model is forced by surface meteorological conditions using the CORE2 surface forcing dataset: 6-h, 2-m air temperature and humidity, and 10-m wind speed are used to calculate turbulent heat flux and surface wind stress, respectively. In addition, daily surface downwelling shortwave and longwave radiation and monthly precipitation are prescribed by CORE2. Temperature and salinity are initialized using a climatology for 2004–08 derived from EN4. The simulation covers 1948–2009 using the Ocean Model Intercomparison Project, phase 2 (OMIP2) protocol (Tsujino et al. 2020; Griffies et al. 2016), where the model starts with zero velocity and runs through five passes of the same forcing with the end state after each pass becoming the initial state of the next pass. We analyze the output from the final pass.

### b. Methods

To account for different dynamical regimes (after Moat et al. 2019), we divide the North Atlantic into four subregions: subpolar west, subpolar east, subtropical west, and subtropical east (Table 2, Fig. 2). We choose large regions because impacts on the atmospheric circulation require coherent anomalies over large length scales (Gastineau and Frankignoul 2015).

We decompose the upper-ocean heat budget beginning with the equation for potential temperature,  $\theta(x, y, z, t)$ , in local Cartesian coordinates, where  $x, y, z$  are the zonal, meridional, and depth coordinates, respectively, and  $t$  is the time:

$$\frac{\partial \theta}{\partial t} = -\mathbf{v} \cdot \nabla \theta + \frac{\partial F}{\partial z}, \quad (1)$$

where  $\mathbf{v}$  is the 3D ocean velocity,  $\nabla$  is the 3D gradient operator, and  $F$  is the vertical diffusive heat flux. We assume horizontal diffusion to be negligible.

Average (1) from surface to depth  $H$ :

$$\frac{\partial \langle \theta \rangle}{\partial t} = \frac{Q_{\text{net}}}{\rho C_p H} - [\mathbf{v}] \cdot \nabla [\theta] - [\mathbf{v}^* \cdot \nabla \theta^*] + \frac{F_{-H}}{H}, \quad (2)$$

where  $Q_{\text{net}}$  is the net surface heat flux,  $\rho$  is the density, and  $C_p$  is the specific heat capacity. Square brackets indicate a depth average (0–1000 m), and variables with an asterisk (\*)

superscript represent a deviation from the depth average,  $a = [a] + a^*$ , where  $[a] = (\int_{-H}^0 a \, dz)/H$ .

The first term on the rhs of (2) represents atmospheric forcing, while the other three terms represent ocean processes. We refer to the sum of these latter three terms on the rhs of (2) as the ocean heat supply. The ocean heat convergence is the sum of terms 2 and 3 on the rhs of (2).

Next, we decompose  $[v]$  and  $[\theta]$  into time-averaged and time-varying quantities where an overbar represents a long-term time average and dashed variables are deviations from the time average,  $a = \bar{a} + a'$ , where  $\bar{a} = (\int_{T_1}^{T_2} a \, dt)/(T_2 - T_1)$ :

$$\begin{aligned} \frac{\partial [\theta]'}{\partial t} = & \frac{Q'_{\text{net}}}{\rho C_p} - [\bar{\mathbf{v}}] \cdot \nabla [\theta]' - [\mathbf{v}'] \cdot \nabla [\bar{\theta}] - ([\mathbf{v}'] \cdot \nabla [\theta]') \\ & - [\bar{\mathbf{v}}] \cdot \nabla [\theta'] - [\mathbf{v}^* \cdot \nabla \theta^*]' + F'_{-H}. \end{aligned} \quad (3)$$

Finally, we perform a 2D spatial average represented by angled brackets,  $\langle a \rangle = (\int_{y_1}^{y_2} \int_{x_1}^{x_2} a \, dx \, dy)/\{(y_2 - y_1)(x_2 - x_1)\}$ .

$$\begin{aligned} \frac{\partial \langle [\theta]' \rangle}{\partial t} = & \frac{\langle Q'_{\text{net}} \rangle}{\rho C_p} - \langle [\bar{\mathbf{v}}] \cdot \nabla [\theta]' \rangle - \langle [\mathbf{v}'] \cdot \nabla [\bar{\theta}] \rangle - (\langle [\mathbf{v}'] \cdot \nabla [\theta]' \rangle \\ & - \langle [\bar{\mathbf{v}}] \cdot \nabla [\theta'] \rangle) - \langle [\mathbf{v}^* \cdot \nabla \theta^*]' \rangle + \langle F'_{-H} \rangle. \end{aligned} \quad (4)$$

The cross terms are expanded as follows where a double asterisk (\*\*) denotes a deviation from the spatial average:

$$\langle [\bar{\mathbf{v}}] \cdot \nabla [\theta]' \rangle = \langle [\bar{\mathbf{v}}] \rangle \cdot \langle \nabla [\theta]' \rangle + \langle [\bar{\mathbf{v}}]^{**} \cdot \nabla [\theta]'^{**} \rangle, \quad (5)$$

$$\langle [\mathbf{v}'] \cdot \nabla [\bar{\theta}] \rangle = \langle [\mathbf{v}'] \rangle \cdot \langle \nabla [\bar{\theta}] \rangle + \langle [\mathbf{v}']^{**} \cdot \nabla [\bar{\theta}]^{**} \rangle. \quad (6)$$

The advective part of the anomalous ocean heat supply can thus be decomposed into six scalar products of a velocity with a temperature gradient. Five terms involve depth-averaged currents and temperature gradients:  $\langle [\bar{\mathbf{v}}] \rangle \cdot \langle \nabla [\theta]' \rangle$ , the time and spatial mean velocity paired with the spatial mean of the anomalous temperature gradient;  $\langle [\bar{\mathbf{v}}]^{**} \cdot \nabla [\theta]'^{**} \rangle$ , the spatial covariance of the mean velocity paired with the anomalous temperature gradient;  $\langle [\mathbf{v}'] \rangle \cdot \langle \nabla [\bar{\theta}] \rangle$ , the spatial mean of the anomalous velocity paired with the time and spatial mean temperature gradient;  $\langle [\mathbf{v}']^{**} \cdot \nabla [\bar{\theta}]^{**} \rangle$ , the spatial covariance of the anomalous velocity paired with the mean temperature gradient; and  $(\langle [\mathbf{v}'] \cdot \nabla [\theta]' \rangle - \langle [\mathbf{v}'] \cdot \nabla [\bar{\theta}] \rangle)$ , the spatial mean of the anomalous velocity paired with the anomalous temperature gradient. Finally, we obtain a contribution from the spatial average of deviations from the vertical average current and depth average (0–1000 m) temperature gradient  $\langle [\mathbf{v}^* \cdot \nabla \theta^*]' \rangle$ . Our decomposition is similar to that of Menary et al. (2015), but

TABLE 2. Definition of North Atlantic subregions.

	Longitude range	Latitude range
Subpolar west	80°–41°W	45°–67°N
Subpolar east	41°W–0°	45°–67°N
Subtropical west	80°–41°W	26°–45°N
Subtropical east	41°W–0°	26°–45°N

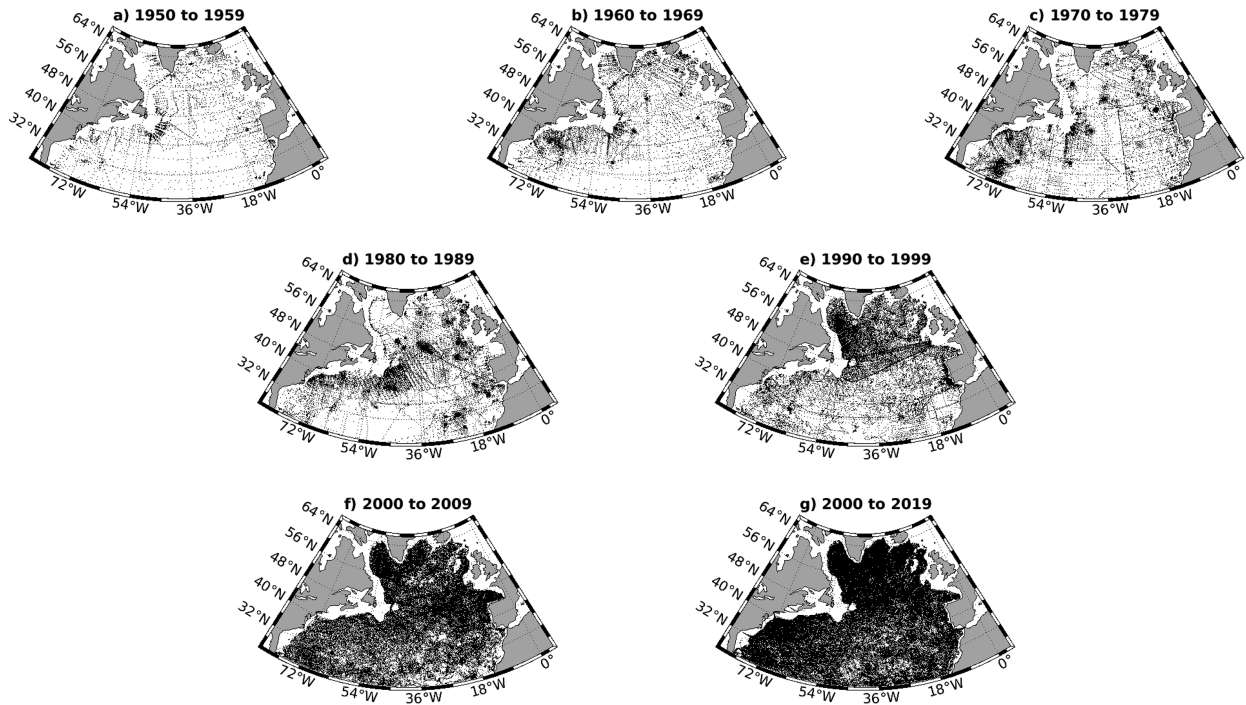


FIG. 1. Locations of temperature–salinity depth profile observations going down to at least 900 m below the surface per decade in the North Atlantic region of our study (80°W–0°, 26°–67°N). Only profiles from the surface to 900 m are shown. (a) 1950–59, (b) 1960–69, (c) 1970–79, (d) 1980–89, (e) 1990–99, (f) 2000–09, and (g) 2010–19.

our method focuses on horizontal heat divergence rather than horizontal heat flux, as we find this aids the physical interpretation of the results as will become clear later (sections 3e–3i). The meaning of the spatial correlation terms is somewhat distinct from the more familiar temporal correlations which can be ascribed to transient eddy and wave activity. The spatial correlations reflect spatially coherent changes in the basin-scale circulation, an example being meandering major current systems such as the Gulf Stream or the North Atlantic Current. Section 3g contains further discussion on this point in the context of the western subpolar region.

To evaluate these terms using observations, we approximate the 3D velocity vector  $\mathbf{v}$  with the 2D geostrophic velocity ( $u_g$  and  $v_g$ ) referenced to a (temporally or spatially variable) level of no motion:

$$u_g = -\frac{1}{f} \frac{\partial \psi}{\partial y}, \quad (7)$$

$$v_g = \frac{1}{f} \frac{\partial \psi}{\partial x}. \quad (8)$$

The streamfunction  $\psi$  is given by

$$\psi = \int_{p_0}^p \alpha \, dp', \quad (9)$$

where  $\alpha$  is the specific volume anomaly (reciprocal of in situ seawater density minus the reciprocal of seawater density at standard temperature and salinity),  $p$  is the hydrostatic

pressure, and  $p_0$  is the pressure at the level of no motion (Pond and Pickard 1983). We take  $p_0$  to be the pressure at 1000 m but investigate the uncertainty introduced by adopting a fixed reference level in section 3d. All variables are filtered to retain periods of 10 years and longer using a Hanning filter.

When analyzing the ocean model simulation, we use not only the full 3D velocity but also the 3D geostrophic velocity derived from the model temperature and salinity fields to assess the importance of ageostrophic motion which is missing from the observed estimates.

As we rely heavily in this paper on the gridded EN4 dataset, based on objective analysis of spatially and temporally inhomogeneous observations of profiles of in situ temperature and salinity, it is appropriate to provide an indication of the data coverage over the upper 1000 m of our chosen spatial region of the North Atlantic (80°W–0°, 26°–67°N; Table 2). We therefore plot the number of temperature–salinity profiles in the dataset within our region of interest which span a depth of at least 900 m (Fig. 1). The spatial density of profiles ranges from relatively sparse (1950–60s) to very dense (2000–10s). Over the whole North Atlantic region of our study, the number of profiles per  $1^\circ \times 1^\circ$  square rises from 2.9 in the 1950s to 67 in the 2010s. There are relatively few extended spatial regions ( $>5^\circ \times 5^\circ$ ) with no data at all. The western subpolar region has relatively sparse coverage southwest of the southern tip of Greenland in the 1970s and rather sparse coverage in the central Labrador Sea in the 1980s. The other major area of sparse coverage is the central subtropical gyre (40°–60°W, 26°–35°N) in the 1980s and to a lesser extent in the 1950s and



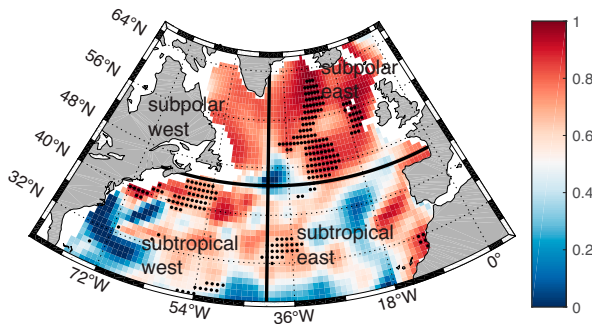


FIG. 2. Correlation coefficient between 0- and 1000-m EN4 OHC and EN4 SST. Both variables are 10-yr low-pass-filtered. Dots indicate values that are significant at the 95% level.

1960s. We therefore flag those regions and periods as carrying the most uncertainty. We note, however, that the western boundary and the path of the North Atlantic Current are well covered in all decades.

3. Results

a. Heat content and AMV

We begin by exploring the relationship between upper-ocean heat content and surface temperature and how this varies spatially. Figure 2 shows simultaneous correlations of decadal filtered 0–1000-m OHC and SST over the period 1950–2020. Both time series were detrended, and autocorrelations were considered in determining the degrees of freedom for significance testing (Emery and Thomson 1997). The variables are strongly positively correlated ( $r$  varies between 0.6 and 0.95) with significant correlation at the 95% level over the eastern subpolar North Atlantic and along the Gulf Stream path. However, correlations are weak ( $r < 0.4$ ) south of about 30°N and anticorrelated close to the western boundary. The northwest corner (~45°N, 40°W) is also a region of anticorrelation. The relatively short time series and decadal filtering mean that the high correlations in the Labrador Sea are not significant at the 95% level; nonetheless, the spatial coherence across the subpolar North Atlantic suggests a physical connection between OHC and SST across the whole region. We conclude that in the northern subtropics and in the subpolar regions, decadal SST variability (and hence atmospheric impacts)

covaries strongly with 0–1000-m OHC. This motivates the focus on OHC variability in this study, i.e., if we can understand and predict the OHC, then since they covary, we can also predict the SST.

b. Ocean heat budget

The observation-based ocean heat budget over 1950–2020 in the four subregions is presented in Table 3. In the subpolar west, subpolar east, and subtropical west, the mean surface heat flux is of order  $-40 \text{ W m}^{-2}$  (negative sign implies heat loss from ocean to atmosphere) and ocean heat supply of order  $+40 \text{ W m}^{-2}$  (positive sign implies convergence into the region) resulting in a small net OHC tendency. In the subtropical east, the mean surface heat flux is positive, and ocean heat supply is negative in contrast to the other regions, and the mean magnitudes of the terms are much smaller, of order  $+4 \text{ W m}^{-2}$ . Interannual and decadal variabilities are larger in ocean heat supply than in surface heat flux.

Figure 3 shows the 1950–2020 decadal filtered heat budget (relative to 1981–2010) only including regions with water depth larger than 1000 m. Net OHC tendency (brown) is a balance between anomalous surface heat flux (green) and ocean heat supply (blue). The OHC and surface flux terms are estimated independently, from ocean observations and atmospheric reanalysis, respectively, while ocean heat supply is obtained as a residual of the other two terms. In all subregions, the three terms are on the order of several watts per square meter. OHC tendency was obtained from three observational datasets (see section 2a, datasets), and the brown shaded area provides an indication of the level of agreement between the datasets which is of order  $1 \text{ W m}^{-2}$ . The ocean heat supply was also estimated based on the three different datasets (blue-shaded area).

Multidecadal variability is present in all subregions. In the subpolar west, there is an alternation of positive and negative OHC tendency (Fig. 3a), with rapid declines in the 1960s and 2000s and a rising trend between the 1970s and 1990s. There is a long period from the mid-1960s to the mid-1980s and another from 1990 to 2015 where ocean heat supply dominates the ocean heat content trend. Subpolar east (Fig. 3b) displays similar behavior with ocean heat supply dominating the OHC tendency even more strongly on decadal time scales and surface heat flux providing a damping. In particular, the warming

TABLE 3. Upper-ocean (surface to 1000 m) heat budgets ( $\text{W m}^{-2}$ ) for the North Atlantic subregions defined in Table 2. SPW = subpolar west, SPE = subpolar east, STW = subtropical west, and STE = subtropical east. The interannual component is isolated by subtracting the decadal filtered variable from the unfiltered data.

	Mean			Interannual std dev			Decadal std dev		
	$Q_{\text{net}}$	Ocean heat supply	Net OHC tendency	$Q_{\text{net}}$	Ocean heat supply	Net OHC tendency	$Q_{\text{net}}$	Ocean heat supply	Net OHC tendency
SPW	−42	42	0	13	19	15	4	5	4
SPE	−44	44	0	7	16	14	2	4	3
STW	−54	55	1	7	17	16	4	4	3
STE	4	−3	1	4	10	9	2	3	1

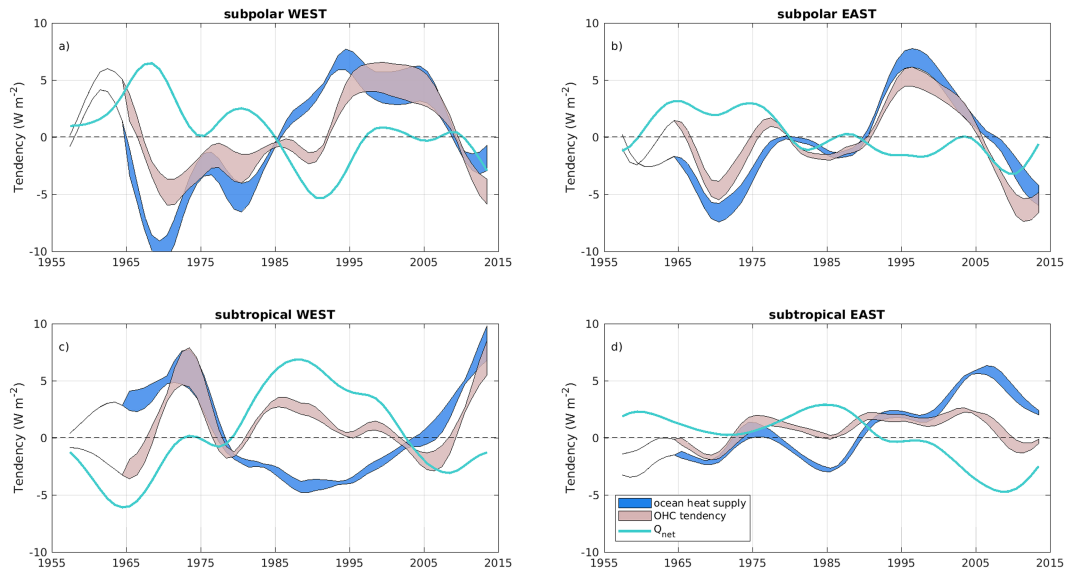


FIG. 3. Decadally filtered heat budget (0–1000-m depth) from observations, 1950–2020, spatially averaged over (a) subpolar west ( $80^{\circ}$ – $41^{\circ}$ W,  $45^{\circ}$ – $67^{\circ}$ N), (b) subpolar east ( $41^{\circ}$ W– $0^{\circ}$ ,  $45^{\circ}$ – $67^{\circ}$ N), (c) subtropical west ( $80^{\circ}$ – $41^{\circ}$ W,  $26^{\circ}$ – $45^{\circ}$ N), and (d) subtropical east ( $41^{\circ}$ W– $0^{\circ}$ ,  $26^{\circ}$ – $45^{\circ}$ N). Brown shading represents a range of estimates of OHC tendency from three different datasets (EN4, ArgoOI, and MOSORA), solid green line represents the net surface heat flux anomaly (with respect to the full period) based on ERA5, and blue shading represents the ocean heat supply implied by the difference between the OHC tendencies and net surface heat flux. All heat budget terms are in watts per square meter.

in the 1990s and the cooling between 1965 and 1975 were driven by changes in ocean heat supply.

In the subtropical west (Fig. 3c), the terms tend to anticorrelate with the corresponding terms in the subpolar west, the most noteworthy difference being that the surface heat flux and ocean heat supply switch sign 5–10 years earlier in the subtropics ( $\sim 1975$  vs  $\sim 1985$  and again  $\sim 2003$  vs  $\sim 2010$ ). There is a long period between 1980 and 2000 where the surface heat flux drives the OHC tendency. Similarly, in the subtropical east (Fig. 3d), the ocean heat supply is most often the same sign as the OHC tendency (hence the driving term), except for the period 1975–90 when surface fluxes drive the net OHC tendency.

We next present (Fig. 4) a heat budget based on the NEMO ocean model (section 2b). The model OHC tendency variability over the North Atlantic is of similar magnitude to the observations ( $\pm 4$ – $5$   $\text{W m}^{-2}$  in all four regions). However, there is a much larger decadal variability in surface heat flux and ocean heat supply in the subpolar regions ( $\pm 20$  vs  $\pm 10$   $\text{W m}^{-2}$  in observations). In the subtropics, the decadal variability in heat flux and ocean heat supply is smaller than the observations ( $\pm 6$  vs  $\pm 10$   $\text{W m}^{-2}$  in the observations). Nonetheless, the evolution of the three terms in the model is similar to observations. In the subpolar regions, we have a rising trend in OHC tendency between the 1970s and 1990s and declining trends from the 1950s to about 1970 and again after 1992. The ocean heat flux (blue) is almost always the same sign as the heat content trend and hence the driving term, whereas the air–sea heat flux is of the opposite sign, qualitatively similar to the observations. In the subtropical west, the

peak in OHC tendency around 1972 (Fig. 4c) is well captured although the later rising trend appears too early, in the early 2000s in the model instead of the late 2000s in observations. In the eastern subtropics, the transition from a negative heat content trend to a positive trend around 1975 is captured by the model. Thus, the model provides a qualitatively plausible simulation of the North Atlantic upper-ocean heat content.

### c. Importance of geostrophic and ageostrophic advection and nonadvective processes

Next, we examine the extent to which horizontal advection by the geostrophic flow accounts for the ocean heat supply on decadal time scales. Due to the high level of agreement between the gridded temperature–salinity datasets (Fig. 3), in this and subsequent analysis, we will focus on just one representative dataset, EN4. We initially choose 1000 m as a reference level for geostrophic calculations. In Fig. 5, the ocean heat supply (blue) is compared with an estimate of the horizontal heat convergence by geostrophic currents (red). There is good correspondence between the two in the subpolar east (Fig. 5b) but poor correspondence in the other three regions. In the subpolar west, the geostrophic heat convergence has a series of peaks and troughs (coinciding with periods of intensified Labrador Sea deep convection in the 1970s, 1990s, and 2010s; see Desbruyères et al. 2020) superimposed on a rising trend. In the subtropical west, the geostrophic convergence makes a large positive excursion around 1970 followed by a large negative excursion around 1995. Ocean heat convergence is anticorrelated with ocean heat supply in the subtropical east.

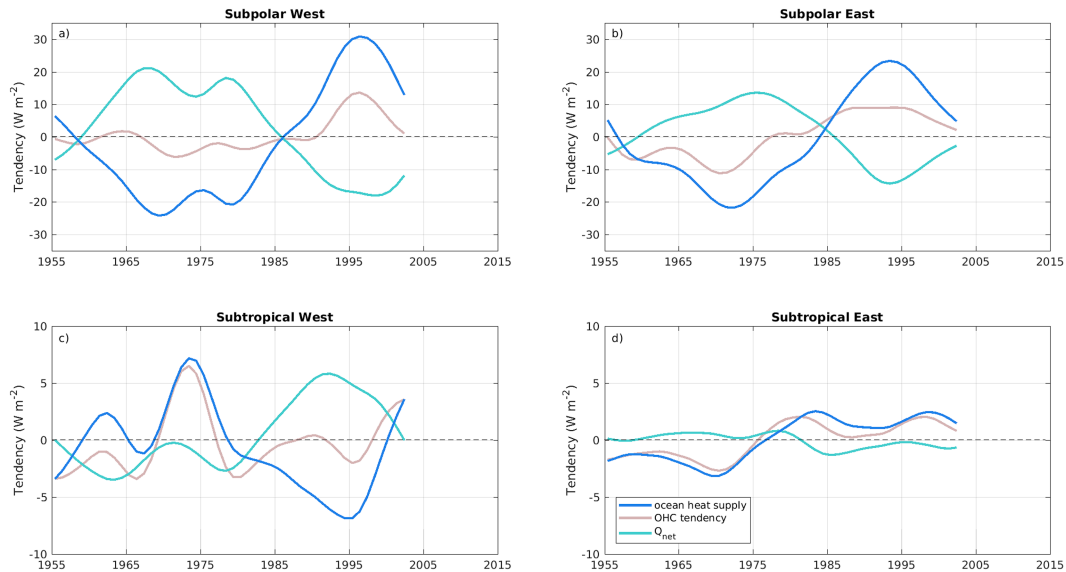


FIG. 4. Decadally filtered heat budget (0–1000-m depth) from the NEMO ORCA025 OMIP2 forced ocean simulation, 1948–2009, spatially averaged over (a) subpolar west ( $80^{\circ}$ – $41^{\circ}$ W,  $45^{\circ}$ – $67^{\circ}$ N), (b) subpolar east ( $41^{\circ}$ W– $0^{\circ}$ ,  $45^{\circ}$ – $67^{\circ}$ N), (c) subtropical west ( $80^{\circ}$ – $41^{\circ}$ W,  $26^{\circ}$ – $45^{\circ}$ N), and (d) subtropical east ( $41^{\circ}$ W– $0^{\circ}$ ,  $26^{\circ}$ – $45^{\circ}$ N). The brown line indicates OHC tendency, the green line indicates net surface heat flux anomaly, and the blue line indicates ocean heat supply.

To understand the relationship between ocean heat convergence and ocean heat supply, we use our NEMO ocean model simulation (Fig. 6) to estimate the magnitude of ageostrophic advection which is difficult to obtain from observations. The model diagnostics allow us to calculate both the net and the

geostrophic ocean heat convergences (red and black, respectively) and compare them with the ocean heat supply (blue). In all regions except subpolar west, the net convergence (red) is very close to the ocean heat supply (blue). In the subpolar west, nonadvective processes (horizontal/vertical

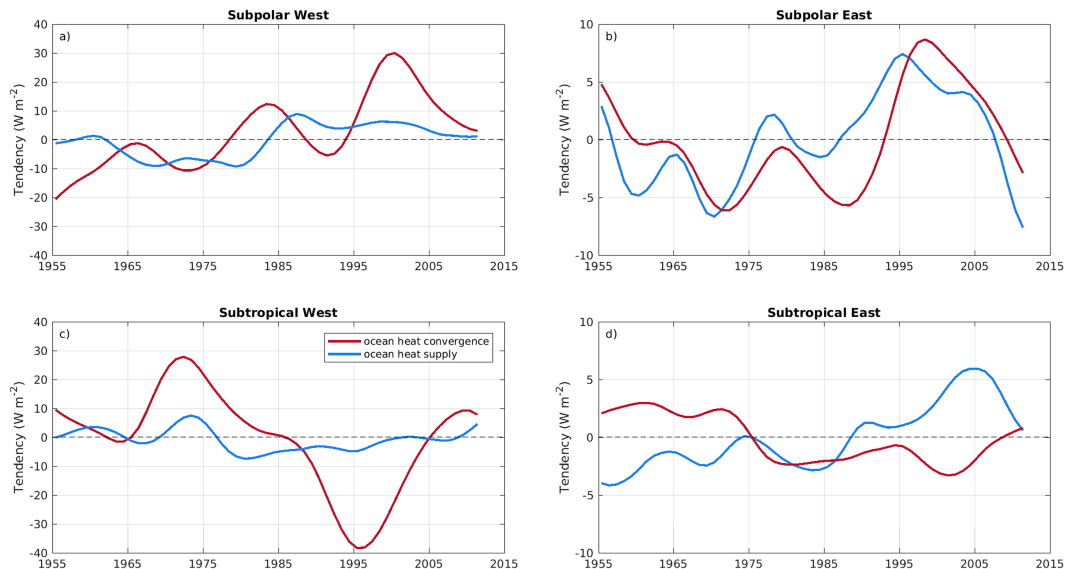


FIG. 5. Comparison of decadally filtered 0–1000-m ocean heat supply ( $\text{W m}^{-2}$ ), 1950–2020, obtained as a residual between ERA5 surface heat flux and EN4 0–1000-m OHC tendency (solid blue line) with decadally filtered 0–1000-m ocean heat convergence based on geostrophic velocities referenced to 1000-m depth calculated from EN4 (solid red line) spatially averaged over (a) subpolar west ( $80^{\circ}$ – $41^{\circ}$ W,  $45^{\circ}$ – $67^{\circ}$ N), (b) subpolar east ( $41^{\circ}$ W– $0^{\circ}$ ,  $45^{\circ}$ – $67^{\circ}$ N), (c) subtropical west ( $80^{\circ}$ – $41^{\circ}$ W,  $26^{\circ}$ – $45^{\circ}$ N), and (d) subtropical east ( $41^{\circ}$ W– $0^{\circ}$ ,  $26^{\circ}$ – $45^{\circ}$ N).

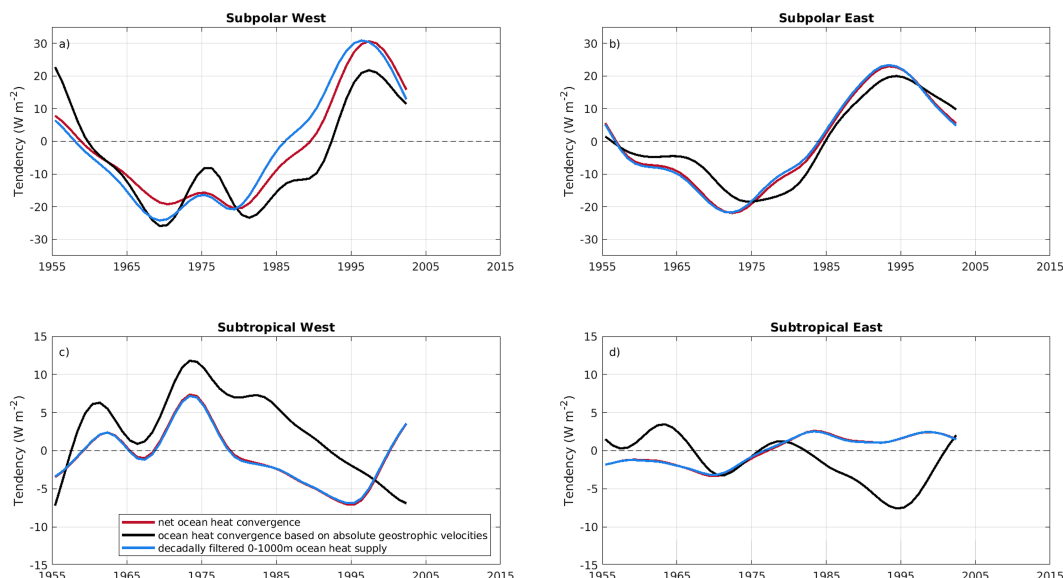


FIG. 6. Comparison of decadal filtered 0–1000-m ocean heat supply ( $\text{W m}^{-2}$ ), 1948–2009, obtained as a residual between surface heat flux and 0–1000-m OHC tendency (solid blue line) with decadal filtered ocean heat convergence based on absolute geostrophic velocities (solid black line), all from the NEMO ORCA025 OMIP2 forced ocean simulation, spatially averaged over (a) subpolar west ( $80^{\circ}$ – $41^{\circ}\text{W}$ ,  $45^{\circ}$ – $67^{\circ}\text{N}$ ), (b) subpolar east ( $41^{\circ}\text{W}$ – $0^{\circ}$ ,  $45^{\circ}$ – $67^{\circ}\text{N}$ ), (c) subtropical west ( $80^{\circ}$ – $41^{\circ}\text{W}$ ,  $26^{\circ}$ – $45^{\circ}\text{N}$ ), and (d) subtropical east ( $41^{\circ}\text{W}$ – $0^{\circ}$ ,  $26^{\circ}$ – $45^{\circ}\text{N}$ ). The solid red line shows decadal filtered ocean heat convergence based on full 3D velocities.

diffusion and entrainment/detrainment) contribute to ocean heat supply but do not dominate. We also note that in both subpolar regions, the geostrophic heat convergence is very similar to the net convergence; hence, ageostrophic currents can be neglected in the heat budget. However, in the subtropical regions, the net and geostrophic convergences are substantially different, implying that ageostrophic currents are of direct importance to the multidecadal heat budget.

#### d. Role of geostrophic reference level in explaining discrepancies between ocean heat supply and geostrophic heat convergence

If we accept the model evidence that ageostrophic currents are unimportant for the subpolar multidecadal heat budget, then the lack of correspondence between geostrophic heat convergence and ocean heat supply in the subpolar west (Fig. 5a) raises questions. In the subtropical regions, ageostrophic currents may explain the discrepancy between the ocean heat supply and the geostrophic convergence seen in the subtropical east (Fig. 5d vs Fig. 4d). However, in the subtropical west, the observations show an overly large geostrophic component in the 1990s (Fig. 5c vs Fig. 4c). These discrepancies suggest the assumption of a fixed 1000-m geostrophic reference level is questionable in the western subregions.

To follow up on this idea, we compare the geostrophic ocean heat convergence calculated using a reference level of 1000 m (i.e., the red lines in Fig. 5) with the absolute geostrophic heat convergence for the period 1993–2020 using absolute surface geostrophic currents based on satellite altimetry as the reference velocity [i.e., using (9), but assuming that the geostrophic current

is equal to satellite-based values at the surface and then integrating downward to 1000 m; Fig. 7, gold lines]. Note that both curves are anomalies from the 1993–2020 mean of the absolute heat convergence. As we are most interested in explaining the decadal variability, we can disregard the large mean offsets between the absolute geostrophic ocean heat convergence and the one based on a 1000-m reference level [up to  $100 \text{ W m}^{-2}$  in the western subregions (Figs. 7a,c) but more like  $20 \text{ W m}^{-2}$  in the eastern subregions (Figs. 7b,d)]. In the subtropical west (Fig. 7a), the heat convergence based on a 1000-m reference level (red line) shows a decline of magnitude  $\sim 20 \text{ W m}^{-2}$  from the year 2000 to 2012 followed by a slight upturn. In contrast, the absolute heat convergence shows a decadal time-scale variation of magnitude about  $25 \text{ W m}^{-2}$ . In the subpolar east, the 1000-m-based heat convergence does capture a decline from the year 2000 onward that is seen in the absolute heat convergence but significantly underestimates the magnitude ( $\sim 15$  vs  $20 \text{ W m}^{-2}$ ). In the subtropical west, the 1000-m reference level is insufficient to capture the steep decline in the absolute heat convergence between 2000 and 2005, the plateau until 2010, and the subsequent further decline to the present. Finally, in the subtropical east, the rising trend seen in the 1000-m-based estimate is not seen in the absolute heat convergence, which instead shows a decadal time scale increase and decrease. We next use the average absolute surface currents from the satellite period (1993–2020) to provide a temporally unvarying reference velocity for the geostrophic calculations (blue line), and as a measure of uncertainty, we also use the surface currents for each individual year of the satellite period (1993, 1994, etc. to 2020) as a temporally unvarying



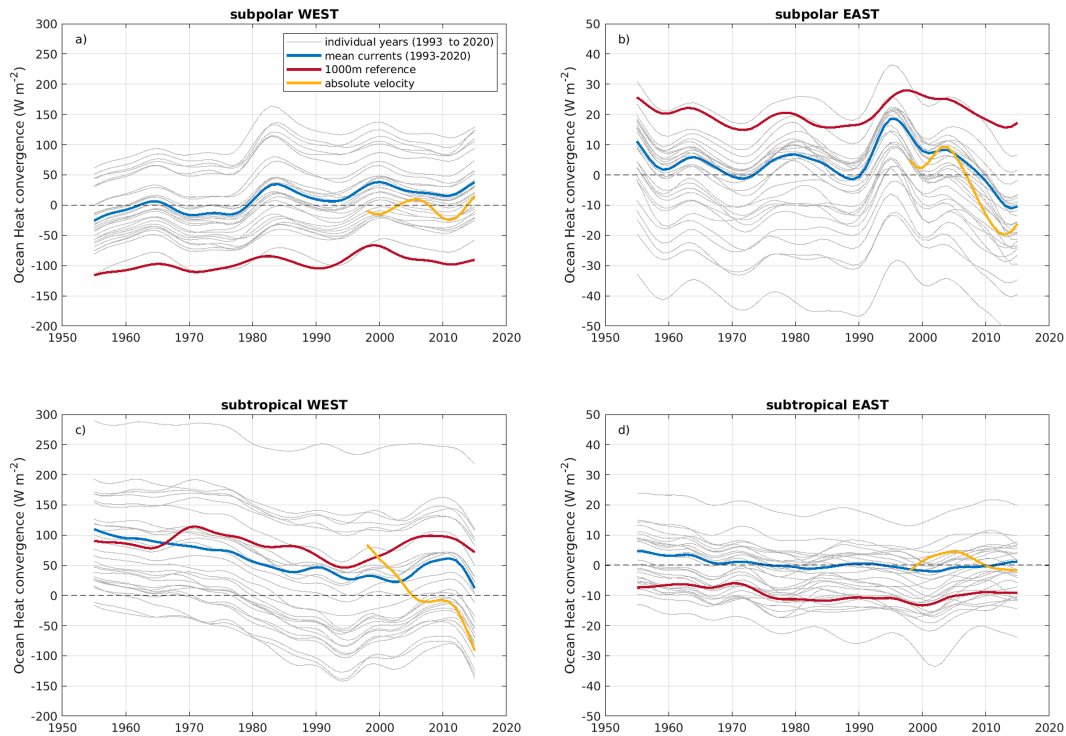


FIG. 7. Dependence of the ocean heat convergence on the choice of the reference level. Absolute geostrophic heat convergence for the period 1993–2020 using absolute surface geostrophic currents based on satellite altimetry (gold lines), surface currents for each individual year of the satellite period (1993–2020) as the reference velocity (gray lines), heat convergence based on a 1000-m reference level (red), and average absolute surface currents from the satellite period (1993–2020) used to provide a reference velocity for the geostrophic calculations (blue line).

reference velocity (gray lines). In all subregions, the gray lines are generally strongly correlated with the blue line, suggesting that the temporal variation of the geostrophic heat convergence in these large regions does not depend very strongly on the choice of reference velocity/level. However, only in the subpolar east region do we get a good match between the blue line and the gold line. In the subpolar east, therefore, using a mean surface reference velocity based on absolute satellite-derived surface currents can be used to reconstruct the ocean heat convergence back to 1950. In contrast in the other three regions, this is not possible, and we require a temporally varying reference velocity to reproduce the absolute currents over the 1993–2020 period. Understanding how the reference velocity should change in earlier epochs is a nontrivial task and requires significant further research.

In summary, taking Figs. 5 and 7 together, we can say that in the subpolar east, the ocean heat convergence based on a 1000-m-based reference level largely explains the ocean heat supply although the amplitude of the variability is probably somewhat too small. In the other regions, the 1000-m-based ocean heat convergence explains a nonnegligible part of the variability, but other processes related to a temporally changing reference velocity (equivalently changing the level of no motion/barotropic velocity) make a significant contribution. In the subtropical regions, ageostrophic heat convergence is likely to play a significant role.

#### e. Approximating geostrophic heat convergence using area and depth-averaged velocity and temperature gradients

Having established the importance of geostrophic ocean heat convergence, we next investigate whether temporal fluctuations in velocity or in temperature gradient dominate the heat convergence or if both processes contribute significantly and how much horizontal variations of velocity and temperature contribute. Figure 8 plots the geostrophic heat convergence (blue) over each region (based on a 1000-m reference level) decomposed into six contributions [section 2b, (4)–(6)]:  $\langle [\mathbf{v}'] \cdot \nabla[\theta'] \rangle$ , the time and spatial mean velocity paired with the spatial mean of the anomalous temperature gradient (solid black);  $\langle [\mathbf{v}']^{**} \cdot \nabla[\theta']^{**} \rangle$ , the spatial covariance of the mean velocity paired with the anomalous temperature gradient (purple triangles);  $\langle [\mathbf{v}']' \cdot \nabla[\theta'] \rangle$ , the spatial mean of the anomalous velocity paired with the time and spatial mean temperature gradient (gold);  $\langle [\mathbf{v}']^{**} \cdot \nabla[\theta']^{**} \rangle$ , the spatial covariance of the anomalous velocity paired with the mean temperature gradient (light red squares); and  $\langle ([\mathbf{v}']' \cdot \nabla[\theta']) - \langle [\mathbf{v}']' \cdot \nabla[\theta']' \rangle \rangle$ , the spatial mean of the anomalous velocity paired with the anomalous temperature gradient (dashed–dot dark red). Finally, we have a contribution from the spatial average of deviations from the depth-averaged current and depth-averaged temperature gradient  $\langle [\mathbf{v}^* \cdot \nabla\theta^*] \rangle$  (dashed black).

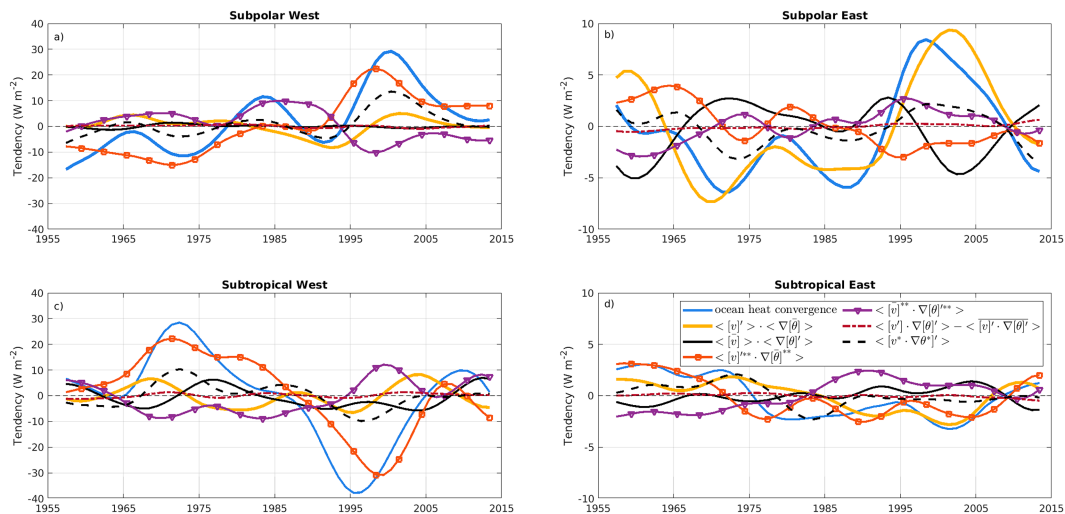


FIG. 8. Decomposition of the observed (EN4 dataset) decadal filtered 0–1000-m ocean heat convergence based on geostrophic velocities, 1950–2020, spatially averaged over (a) subpolar west ( $80^{\circ}$ – $41^{\circ}$ W,  $45^{\circ}$ – $67^{\circ}$ N), (b) subpolar east ( $41^{\circ}$ W– $0^{\circ}$ ,  $45^{\circ}$ – $67^{\circ}$ N), (c) subtropical west ( $80^{\circ}$ – $41^{\circ}$ W,  $26^{\circ}$ – $45^{\circ}$ N), and (d) subtropical east ( $41^{\circ}$ W– $0^{\circ}$ ,  $26^{\circ}$ – $45^{\circ}$ N). Blue, ocean heat convergence; solid black, spatially averaged time-mean velocity acting on spatially averaged anomalous temperature gradient; dashed black, vertical covariance term; gold, spatially averaged anomalous velocity acting on spatially averaged time-mean temperature gradient; dark red dashed-dotted, spatial average of anomalous velocity acting on anomalous temperature gradient; purple triangles, spatial covariance of time-mean velocity acting on spatially averaged anomalous temperature gradient; and red squares, spatial covariance of anomalous velocity acting on spatially averaged time-mean temperature gradient. All terms are in watts per square meter. The reference level for geostrophic velocities is referenced to 1000-m depth.

Recall that in the subtropical east, the geostrophic ocean heat convergence more or less explains the overall ocean heat supply. In this region (Fig. 8b), correlated variations of horizontal and vertical spatial anomalies in velocity fields and temperature gradients are of lesser importance, and the ocean heat supply over the whole region is well characterized by using the spatially and depth-averaged anomalous velocity and mean temperature gradient to determine the heat convergence (gold). This term is opposed by the spatially and depth-averaged mean velocity acting on the anomalous temperature gradient (solid black) and reinforced by vertical fluctuations of velocity and temperature gradient (dashed black). The spatial correlation terms (purple triangles and light red circles) oppose each other and tend to cancel out. The least important term is the correlation between anomalous velocity and anomalous temperature gradient (dark red squares).

In the subpolar west (Fig. 8a), correlated horizontal spatial variations of anomalous currents and the mean temperature gradient (light red circles) dominate the geostrophic ocean heat convergence (blue), and the corresponding spatial mean term (gold) is a relatively small term. The vertical correlation term (correlated vertical variations in the velocity field and the temperature gradient—dashed black) also plays a significant role, increasing with time and related to the decadal alternation between periods of Labrador Sea deep convection (Desbruyères et al. 2020). Horizontal spatial correlations of mean currents and anomalous temperature gradients (purple triangles) act in opposition to these terms.

In the subtropical west (Fig. 8c), the two horizontal correlation terms are again found to dominate. The horizontal correlations of the anomalous velocity and the mean temperature gradient (light red circles) explain most of the geostrophic ocean heat convergence and are opposed by horizontal correlations between the mean velocity and the anomalous temperature gradient (purple triangles).

The subtropical east (Fig. 8d) presents a more complex picture with different terms important at different times. However, the terms involving anomalous velocity acting on mean temperature gradients [both spatial mean (gold) and correlations (light red circles)] and the vertical correlation term (dashed black) are the drivers. They are opposed by the terms involving the mean velocity acting on the anomalous temperature gradient (solid black and purple triangles).

#### f. The role of anomalous velocity in the temporal variations in geostrophic heat convergence

Reverting to a 2D perspective (Fig. 9), we plot correlations between the net heat convergence term (excluding vertical correlations),  $[\bar{v}] \cdot \nabla[\theta]' + [\bar{v}'] \cdot \nabla[\bar{\theta}] + ([\bar{v}'] \cdot \nabla[\theta]' - [\bar{v}]' \cdot \nabla[\bar{\theta}']')$ , and each of the components: anomalous current times mean temperature gradient ( $[\bar{v}'] \cdot \nabla[\bar{\theta}]'$ ; Fig. 9a), mean current times anomalous temperature gradient ( $[\bar{v}] \cdot \nabla[\theta]'$ ; Fig. 9b), and anomalous current times anomalous temperature gradient ( $[\bar{v}'] \cdot \nabla[\theta]' - [\bar{v}]' \cdot \nabla[\bar{\theta}']'$ ; Fig. 9c). Figure 9a (anomalous current  $\times$  mean gradient) is dominated by positive correlations, and a large part of the variance in the ocean heat supply on decadal (and longer) time scales is caused by

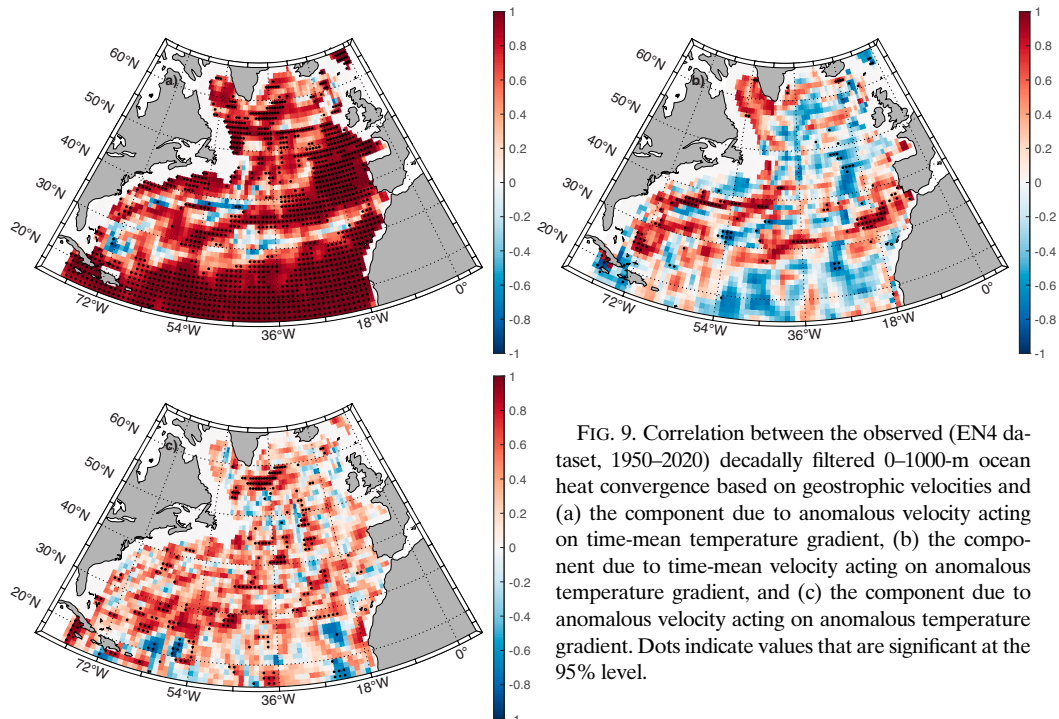


FIG. 9. Correlation between the observed (EN4 dataset, 1950–2020) decadal filtered 0–1000-m ocean heat convergence based on geostrophic velocities and (a) the component due to anomalous velocity acting on time-mean temperature gradient, (b) the component due to time-mean velocity acting on anomalous temperature gradient, and (c) the component due to anomalous velocity acting on anomalous temperature gradient. Dots indicate values that are significant at the 95% level.

fluctuations in the current alone. Conversely, there are two elongated regions where the correlation is small/negative, and these seem to be associated with the Gulf Stream/North Atlantic Current and the subtropical return flow. Figure 9b (mean current  $\times$  anomalous gradient) is predominantly small/negative and only positive in the regions with strong currents. This explains the balances over the wider areas in Fig. 8, in particular the general anticorrelation between the terms involving the anomalous velocity/mean temperature gradient versus those involving the mean velocity/anomalous temperature gradient. The correlation between the net convergence term and the anomalous velocity times anomalous temperature gradient is shown in Fig. 9c which reveals weak correlations and little coherence over large spatial scales compared to the other terms. Exceptions to this include the central subpolar gyre ( $\sim 55^\circ\text{N}$ ,  $36^\circ\text{W}$ ) and the central subtropical gyre ( $\sim 30^\circ\text{N}$ ,  $40^\circ$ – $60^\circ\text{W}$ ). The reasons for significant correlations in these regions are not immediately clear but may be related to eddy processes.

*g. The role of anomalous geostrophic currents and the mean temperature gradient in determining the multidecadal variations in ocean heat convergence*

Having established the importance of anomalous currents acting on the mean temperature gradient, we plot current vectors (blue) for every year in each subregion along with corresponding mean (negative) temperature gradient (red) vectors (Fig. 10). The key to understanding how these two vectors determine the ocean heat convergence (and hence ocean heat supply) is that the scalar product of two vectors depends on both the magnitudes of the vectors and the angle between them. Zero convergence occurs when the vectors are at right

angles to each other (e.g., around 1994 and 2008 in the eastern subpolar region). Positive convergence generally occurs when the velocity is at an acute angle ( $<90^\circ$ ) to the mean temperature gradient (1960s, 1990s, and 2000s), and negative convergence occurs when the angle is obtuse ( $>90^\circ$ ) (1970s, 1980s, and 2010s). Extremes of ocean heat convergence occur when the two vectors are aligned ( $0^\circ$ , e.g., 1997) or oppositely aligned ( $180^\circ$ , e.g., 1988).

The standout feature of the vector plots is the tendency of the velocity vector to rotate anticlockwise, seen, for example, in the subpolar east in the 1960s and 1990s, subpolar west in the 1990s, and subtropical west around 1970 and again around 2010 ( $\sim 10$ -yr phase difference with the subpolar regions). In the subtropical east, the phenomenon occurs around 1977, a further  $\sim 7$ -yr phase difference from the western subtropics. The periods with fast anticlockwise rotation are relatively short and alternate with periods of negative (southward directed) currents which gradually turn anticlockwise in the 1970s to early 1980s in the subpolar west, stretching into the 1990s in the subpolar east, the 1980s to early 1990s in the subtropical west, and the 1990s–2000s in the subtropical east.

The anticlockwise rotation of the mean velocity vector can be seen more clearly in Fig. 11 where the velocity vector for subtropical east (blue arrows) is normalized to 1 unit in all years. Focusing on the 1990s, we see the velocity vector initially pointing southeastward and at an obtuse angle to the mean temperature gradient (red arrow), implying a negative anomaly in the ocean heat convergence. The velocity vector tracks anticlockwise year by year until it is almost aligned with the mean temperature gradient in 1997, implying maximum ocean heat convergence in this year. In subsequent

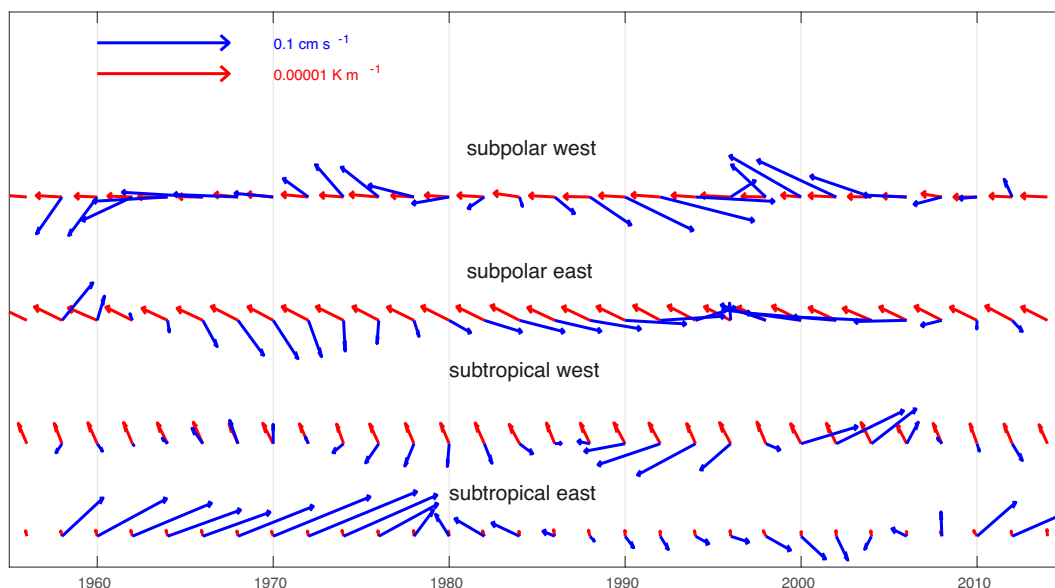


FIG. 10. Vectors of observed (EN4) decadal averaged, 0–1000-m depth, anomalous geostrophic velocity (blue) and (negative) time-mean temperature gradient (red) spatially averaged over subpolar west ( $80^{\circ}$ – $41^{\circ}$ W,  $45^{\circ}$ – $67^{\circ}$ N), subpolar east ( $41^{\circ}$ W– $0^{\circ}$ ,  $45^{\circ}$ – $67^{\circ}$ N), subtropical west ( $80^{\circ}$ – $41^{\circ}$ W,  $26^{\circ}$ – $45^{\circ}$ N), and subtropical east ( $41^{\circ}$ W– $0^{\circ}$ ,  $26^{\circ}$ – $45^{\circ}$ N) for the period 1950–2020. The reference level for geostrophic velocities is referenced to 1000-m depth.

years, the velocity vector continues tracking anticlockwise. In 2000, there is a near right angle between the velocity vector and the mean temperature gradient implying zero ocean heat convergence.

The decadal swings in ocean heat supply are therefore a manifestation of the rotating velocity vector periodically coming into alignment with the mean horizontal temperature gradient. The process applies at most individual locations, but averaging up to the subregion scale would be affected by the spatial covariance between the horizontal velocity and the

temperature gradient. In the subpolar east, the spatial covariance terms are relatively small and cancel each other (Fig. 7), but as mentioned earlier, they are more important in the other three subregions.

The spatial correlation term involving anomalous velocity and time-mean temperature gradient is significant in three of four subregions. Figure 12a shows anomalous 0–1000-m velocity vectors (blue) and time-mean temperature gradient vectors (red) spatially averaged over 0–1000-m depth for the year 1990 in the subpolar west. In 1990, the contribution of the

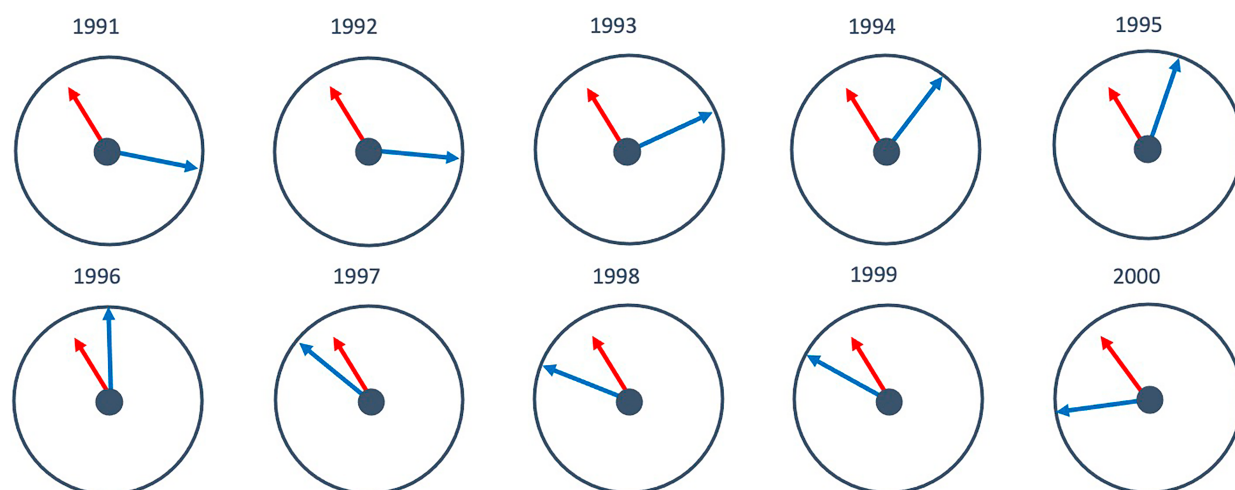


FIG. 11. Illustration of anticlockwise rotation of the velocity vector in the subpolar east region. Anomalous geostrophic velocity is shown in blue, and (negative) time-mean temperature gradient is shown in red. The reference level for geostrophic velocities is referenced to 1000-m depth.



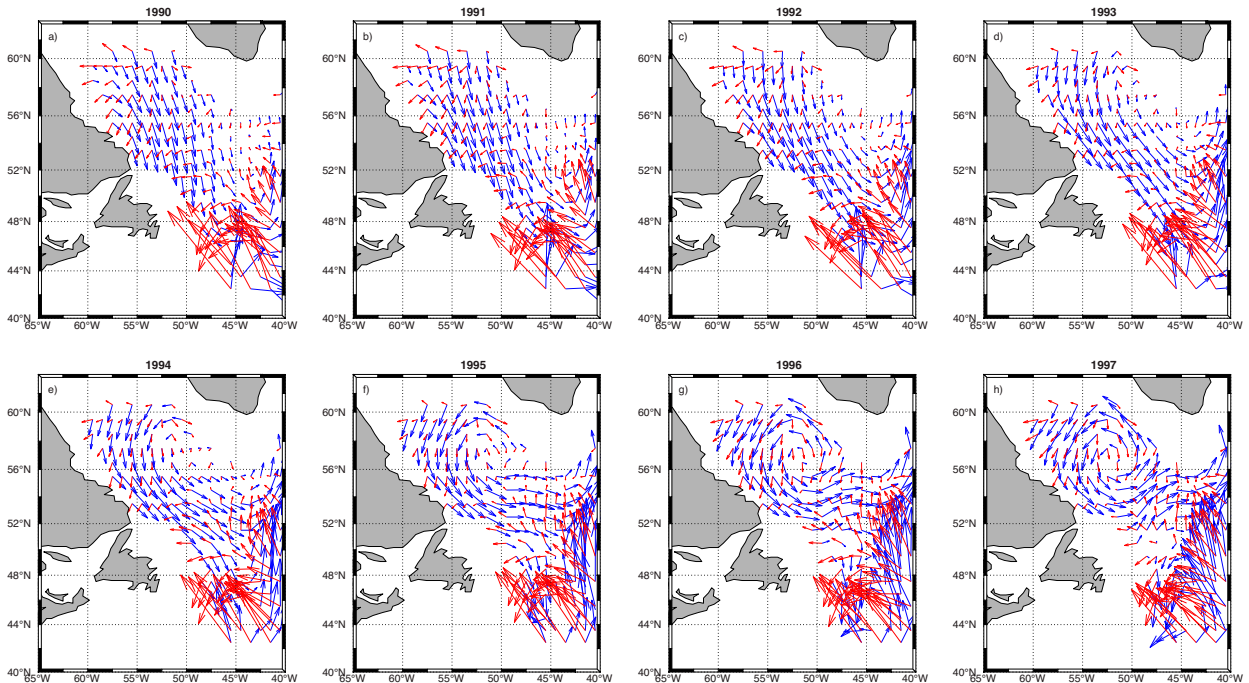


FIG. 12. Vectors of observed (EN4) decadal averaged, 0–1000-m depth, anomalous geostrophic velocity (blue) and (negative) time-mean temperature gradient (red) for (a)–(h) 1990–97. The reference level for geostrophic velocities is referenced to 1000-m depth.

$[\mathbf{v}]^{***} \cdot \nabla[\theta]^{**}$  term spatially averaged over the region was about  $0 \text{ W m}^{-2}$  and increased to about  $+20 \text{ W m}^{-2}$  over the next 7 years (Fig. 8a). The magnitudes of both the anomalous velocities and the mean temperature gradient are largest in the southern part of the domain (south of  $\sim 52^\circ\text{N}$ ) and smallest in the north. The (negative) temperature gradient is also oriented southwest in the north versus more northwest in the south. Over 1991–97 (Figs. 12b–h), the current vectors in the north rotate clockwise, tending to bring the currents more in alignment with the temperature gradient around 1995, whereas in the south, the currents rotate anticlockwise (as in the eastern domain) and are well out of alignment by 1995. The circulation regime changes from a predominantly southward flow to a cyclonic circulation likely associated with the onset of deep convection in the Labrador Sea in the mid-1990s. The large currents to the extreme southeast do not change much until 1995 when they begin to swing anticlockwise. The systematic spatial variation of the amplitude and phase of the current with respect to the temperature gradient and their changes with time generate the time-varying spatial correlation term. Similar behavior occurs in the subtropics (not shown). Thus, the same mechanism operates in all four subregions, anomalous velocity vectors rotating in and out of alignment with the mean temperature gradient, but manifests differently where there is a large correlated spatial gradient in the magnitudes and phases of the two vectors.

#### h. Mechanism of decadal ocean circulation variability

The spatial average of the geostrophic current over the subregions only depends on the streamfunction along the boundaries.

Thus, we hypothesize that a propagating perturbation with a large horizontal length scale is responsible for the observed velocity variations. We test this hypothesis by plotting the decadal filtered geostrophic streamfunction (referenced to 1000-m depth) at four key points in the historical time series corresponding to the two maxima (1956 and 1996) and two minima (1972 and 2013) in meridional velocity. In 1956 (Fig. 13a), the streamfunction anomaly is negative at Cape Farewell ( $\sim 41^\circ\text{W}$ ) and positive at the eastern boundary consistent with a strong positive meridional velocity. This contrasts with the situation in 1972 (Fig. 13b) when there are positive anomalies at Cape Farewell and negative anomalies at the eastern boundary, with an implied strongly negative meridional velocity. Note the thick band of negative anomalies stretching from the East Coast of the United States all the way to the British Isles and Iceland. Twenty-four years later, in 1996 (Fig. 13c), the situation has reversed with a stripe of positive anomalies now stretching from southwest to northeast, sandwiched between two areas of negative anomalies. Finally, in 2013 (Fig. 13d), we have a situation reminiscent of 1972 with again a band of negative anomalies stretching from the United States to the British Isles (albeit much thinner in width), flanked by two extensive areas of positive anomalies. While these observed anomalies do not display precisely repeating patterns, the reversals on time scales of 18–20 years (hence a period of order 36–40 years) and the preferred southwest to northeast orientation are striking.

Figure 13 shows periodic reversals in the streamfunction patterns but does not in itself demonstrate propagation. Figure 14 shows distance–time diagrams of the 0–1000-m velocity (the component oriented southwest to northeast, along the streamfunction

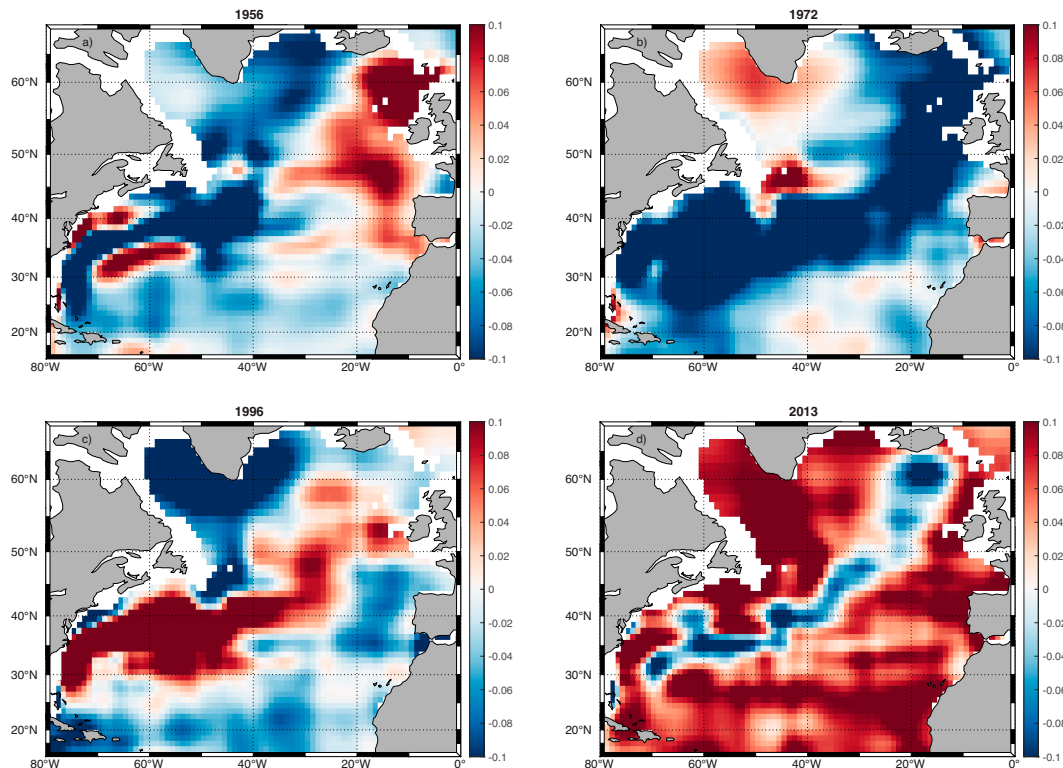


FIG. 13. Representative plots of decadal filtered geostrophic streamfunction anomaly vertically averaged over 0–1000-m depth ( $\text{m}^2 \text{s}^{-2}$ ) at key points of the multidecadal cycle: (a) 1956, (b) 1972, (c) 1996, and (d) 2013. The streamfunction is calculated from the EN4 gridded temperature–salinity dataset, using a fixed reference level of 1000-m depth. Anomalies are calculated relative to the 1950–2020 mean. Regions with water depth less than 1000 m are excluded from the analysis.

ridges seen in Fig. 11, as we anticipate there may be propagation perpendicular to this direction. Figure 14a shows this component of velocity along the 56°N latitude line, while Fig. 14b is along 61°N. In Fig. 14a, a line of positive anomalies catches the eye, originating around 1980 at  $\sim 30^\circ\text{W}$  and reaching 55°W in 2010 (propagation speed  $\sim 1.6 \times 10^{-3} \text{ m s}^{-1}$ ). A fainter negative

anomaly originates in about 1965 at  $\sim 35^\circ\text{W}$  and arrives at 55°W around 1995. Anomalies with similar start and endpoints appear at 61°N (Fig. 14b). The anomalies at this latitude appear to reach the east coast of Greenland ( $\sim 41^\circ\text{W}$ ) and then continue to propagate westward from the west coast of Greenland to the East Coast of North America. There is also an earlier anomaly at this

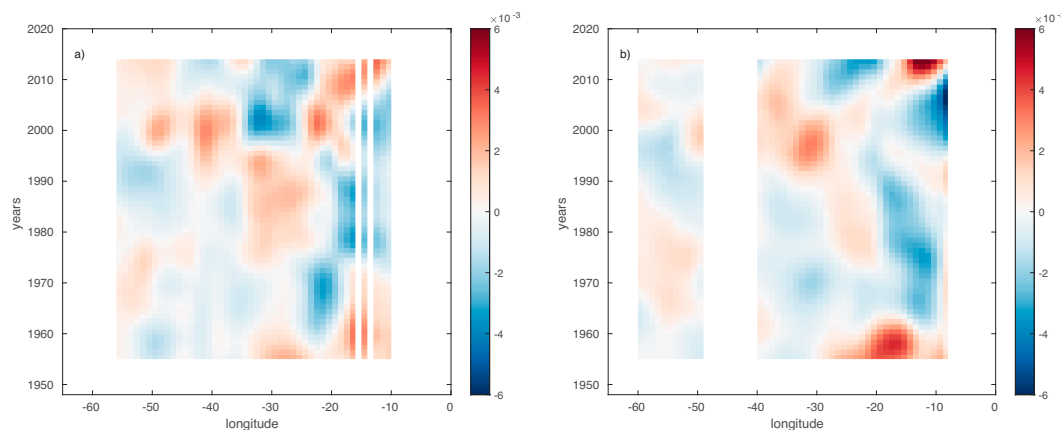


FIG. 14. Latitude–time diagram showing the 0–1000-m geostrophic velocity ( $\text{m s}^{-1}$ ) (component oriented from southwest to northeast) at (a) 56°N and (b) 61°N. The assumed level of no motion for the geostrophic calculation is 1000 m.

latitude which originates in 1960 at 41°N on the east coast of Greenland and arrives at the North American coast (~60°W) around 1980.

This behavior is reminiscent of a wave of pressure perturbation moving westward, or northwestward, albeit with a very large wavelength, long period (~30–40 years), and low frequency. A long Rossby wave has the phase speed:

$$u_{\beta} = \beta R_d^2, \quad (10)$$

where  $\beta = \partial f / \partial y$  is the variation of Coriolis parameter  $f$  with latitude and  $R_d$  is the internal Rossby radius. At subpolar latitudes (~55°N),  $R_d \sim 10$  km and  $\beta = 1.3 \times 10^{-11} \text{ m}^{-1} \text{ s}^{-1}$  giving a phase speed of  $0.0013 \text{ m s}^{-1}$ . For a wavelength of ~4000 km, the basin width at this latitude, this yields a period of 97 years, which is too slow to explain the observed time scale of variability (30–40 years).

It is well known that classical long baroclinic Rossby waves of the type seen in satellite altimetry from the 1990s onward are about a factor of two or more faster than linear theory predicts (e.g., Chelton and Schlax 1996; Killworth et al. 1997) which would bring them more into line with the observed period of the variability. However, satellite observations show typical wavelengths at subtropical to subpolar latitudes of a few 100 km which is quite short compared to the observed length scales (Fig. 13), and modeled and observed waves travel too fast to explain the multidecadal variability we focus on here. For example, Wang et al. (2022) find combinations of  $\beta$ -generated and topographically generated Rossby waves take 4–10 years to cross the Atlantic basin at ~60°N. Clearly, these faster propagating waves are present and do affect the variability on interannual to multiyear time scales.

Another possibility is a thermal Rossby wave (Sévellec and Fedorov 2013, 2015; Gastineau et al. 2018), which propagates by geostrophic self-advection along a north–south temperature gradient. The ratio of the phase speed,  $u_{\text{thermal}}$ , of a thermal Rossby wave to the “ordinary” Rossby wave speed,  $u_{\beta}$ , is given by the following formula (derived from Sévellec and Fedorov 2013), neglecting advection by mean currents (usually canceled or exceeded by the geostrophic self-advection, the so-called “non-Doppler” effect; Sévellec and Huck 2015):

$$u_{\text{thermal}}/u_{\beta} = \frac{2f}{\beta H} \frac{\partial \bar{T} / \partial y}{\partial \bar{T} / \partial z}, \quad (11)$$

where  $H$  is the depth of the upper layer (surface to 1000 m) and  $\partial \bar{T} / \partial y$  and  $\partial \bar{T} / \partial z$  are the mean meridional and vertical temperature gradients, respectively. Typical values for the eastern subpolar gyre based on the EN4 dataset yield a thermal Rossby wave speed ~3 times faster than the ordinary Rossby wave ( $u_{\text{thermal}} \sim 3.9 \times 10^{-3} \text{ m s}^{-1}$ ) and hence a period ~3 times smaller, bringing it into the range of 97/3 or ~32 years.

Consider an idealized westward propagating thermal Rossby wave, streamfunction  $\psi$ , and amplitude  $\psi_0$ :

$$\psi = \psi_0 \sin(kx + ly - \omega t), \quad (12)$$

$$\omega = \frac{-\beta^* k}{(k^2 + l^2 + 1/R_d^2)}, \quad (13)$$

where  $\beta^* > \beta$  represents the effect of a north–south temperature gradient.

We initially examine the purely zonally propagating case:  $k = 2\pi/4000$  km and  $l = 0$  in the subpolar east subregion (Fig. 15a). The spatial average velocity vector in the region delimited by the black box is shown in Fig. 15b. Since this wave has no meridional structure,  $u = 0$  identically. The spatial average velocity in the box is therefore simply the difference in the average streamfunction at the meridional boundaries of the box and the rise, fall, and periodic reversal of the velocity is due to the fact that the wave has a different phase at the west of the box than at the east and the difference in the amplitude of the wave varies as it passes through the box. This simple model does not reproduce the rotation of the current vector seen in observations but reproduces the periodic phase reversals at about the right frequency. Next, we add meridional structure to the streamfunction by setting  $k = 2\pi/4000$  km and  $l = -2\pi/2000$  km (Fig. 15c), so the wave propagates to the northwest. The phase propagation of the tilted streamlines results in related changes between  $u$  and  $v$  (Fig. 15d). However, the sense of rotation is incorrect since the changes in  $u$  always precede the changes in  $v$  due to the orientation of the streamfunction isolines. To reproduce the observations, we add the two previous waves (Figs. 15e,f) and recover both the time scale and the sense of rotation of the velocity vector. Figures 15e and 15f seem sufficiently similar to Figs. 10, 11, and 13 that the Rossby wave mechanism seems plausible; however, the physical reasons behind the need for two superimposed waves require further study. Some other features of Fig. 10 require further explanation; for example, we do not fully understand the relationship between the direction of the temperature gradient and the preferred direction of the velocity vector and why the latter is different in higher versus lower latitudes (southwest to northeast in the subpolar regions and southeast to northwest in the subtropical regions). We emphasize that Fig. 15 is a kind of fitting exercise and does not in itself prove that the underlying variability is due to Rossby wave propagation, which would require further development of thermal Rossby wave theory plus a more thorough investigation of the mechanism in model simulations; however, it suggests a simple and plausible explanation for the observations.

#### i. Relationship of subpolar OHC variability with the AMOC

Next, we examine the relationship between the AMOC at 26°N and subpolar OHC variability, using the NEMO model simulation, due to the shortness of the observational time series. Figure 16a shows the OHC tendency during a decade when the decadal filtered AMOC was less than one standard deviation from its mean (see Fig. 16d) minus the tendency when the AMOC was greater than one standard deviation from its mean. Figures 16b and 16c similarly show





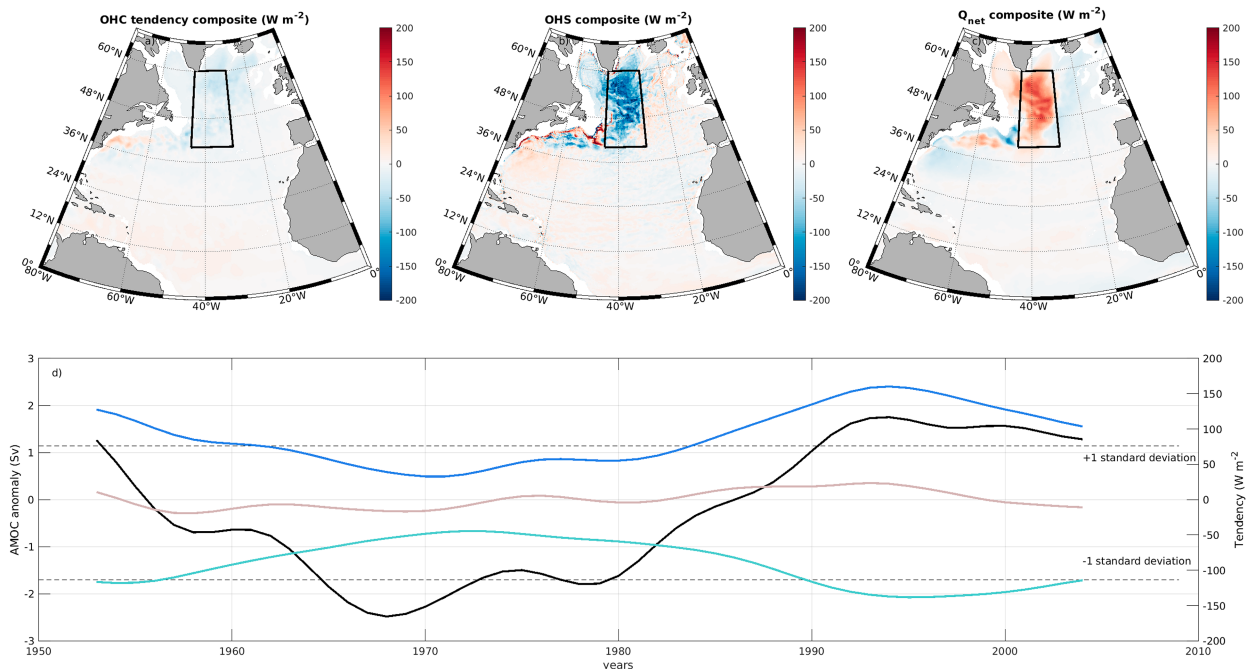


FIG. 16. (a) Difference between OHC tendencies when the decadal filtered AMOC at 26°N was less than one standard deviation from the mean and greater than one standard deviation from the mean; (b) as in (a), but for considering the ocean heat supply; (c) as in (a), but for considering the net surface heat flux; and (d) time series of decadal filtered AMOC anomaly (black) relative to the 1948–2009 mean AMOC. The average OHC (brown), OHS (blue), and  $Q_{\text{net}}$  (green) are shown for the box indicated in the upper panels. Horizontal dotted lines show the AMOC maximum and minimum used to calculate the difference plots in (a)–(c). All plots are based on the NEMO-CICE 1/4° forced ocean simulation.

(indicated in Figs. 16a–c by the solid black outline). Averages of the tendency terms in these regions are plotted alongside the AMOC index in Fig. 16d to further characterize the relationship between the AMOC and the budget terms. The ocean heat supply (blue) is seen to vary in phase with the AMOC, while the surface flux term varies in antiphase.

The correlations can be interpreted in conjunction with Fig. 13. Since the AMOC is a manifestation of the pressure difference across the boundary, it will change in step with the progress of the thermal Rossby waves across the subpolar gyre.

The changes in the AMOC represent a change in the zonally averaged meridional velocity and as such will affect the ocean heat divergence and will be included in Fig. 10a, for example. However, the lack of long-term AMOC observations makes it difficult to disentangle its impact, and further model analysis is required.

#### 4. Summary and discussion

We have constructed a three-term multidecadal upper ocean heat budget for the North Atlantic whereby ocean heat content tendency equals ocean heat supply plus surface heat flux input to determine to what extent the ocean heat supply is explained by ocean heat transport convergence. Atmospheric reanalysis products provide surface heat flux estimates, while the ocean heat convergence is obtained using geostrophic currents and the ocean temperature gradient from gridded in situ

ocean observations. Ocean heat content tendency is calculated from the same ocean observations. A fixed 1000-m reference level is used for geostrophic calculations, but we also quantify the uncertainty due to this assumption by comparing it with satellite-based estimates of absolute geostrophic heat convergence for the 1993–2020 period.

We demonstrate that variations in horizontal ocean heat transport divergence drive multidecadal changes in North Atlantic upper-ocean heat content. In the subpolar North Atlantic, ocean heat transport divergence variations are the primary cause of such changes. Further decomposition of the ocean heat supply reveals that the dominant process is the advection of the mean temperature gradient by anomalous geostrophic currents, driven by horizontal pressure gradients. In the subtropical North Atlantic, advection by geostrophic currents is important, but ageostrophic currents play an equal role. The surface heat flux remains an important contributor throughout the North Atlantic but represents a passive feedback process.

In the subpolar gyre, we find a wavelike basin-scale northwestward progression of geostrophic velocity anomalies. The northwestward progression can be modeled by a combination of two long (several thousand kilometers) wavelength propagating plane waves. The wave speed ( $\sim 0.004 \text{ m s}^{-1}$ ) is faster than a long Rossby wave of the same wavelength and is more characteristic of a thermal Rossby wave driven by geostrophic self-advection due to the presence of a meridional temperature gradient. The two waves consist of one propagating

purely westward with zero meridional wavenumber and another propagating northwestward with a zonal and a meridional wavenumber.

The wavelike progression is reflected in the anticlockwise rotation of the geostrophic velocity vectors throughout large parts of the North Atlantic. The explanation for observed multidecadal changes in heat content tendency is that the velocity vector periodically aligns with the mean temperature gradient. This is very marked in the eastern subpolar gyre where just two vectors, the anomalous geostrophic velocity and the mean temperature gradient, determine the evolution of the heat content tendency over a very large geographical region. These two vectors are therefore potentially a very useful predictor of near-term changes to the ocean heat content and SST in the subpolar gyre. In the western subpolar gyre, large correlated spatial variations in both temperature gradient and the magnitude and phase of the anomalous velocity make predictions more difficult, but nonetheless, the anomalous velocity linked to the wave propagation determines the heat content tendency to a large extent. In the subtropics, more processes are involved, including ageostrophic advection of heat, advection of temperature anomalies by the mean current, and the impact of vertical structure.

The trigger for the subpolar variability remains a big question. If a damped thermal Rossby wave is the explanation for the variability, then there would need to be some mechanism to excite this—for example, random atmospheric weather variability, mesoscale eddies, or perhaps boundary wave propagation (Gastineau et al. 2018). It remains unclear why there would be two waves excited and what sets the amplitude of the variability. There is, however, also the possibility that the Rossby wave represents an unstable mode, a consequence of generalized baroclinic instability (Sévellec and Huck 2015). In this situation, the waves could be self-sustaining. Further investigation is required to discriminate between the two possibilities.

We find a good correspondence between ocean heat supply and the AMOC, especially in the subpolar gyre; however, it remains unclear how much the AMOC anomalies are a cause rather than an effect of the wave propagation in the gyre. Nonetheless, the AMOC remains an excellent predictor of the subpolar gyre heat content and vice versa.

The eastern subpolar region emerges as the most predictable region, and there are interesting implications for climate change projections. Any changes which impact the horizontal temperature gradient could affect both the amplitude and time scale of decadal variability in the SPG, for example.

A novel aspect is the combination of the model and the observation-based heat budget to constrain the geostrophic reference level. We conclude that 1000 m is a realistic choice for reference level in the eastern North Atlantic (cf. with e.g., Stramma 1984, who used classical hydrographic methods to deduce reference levels of 1200–1500 m in the eastern subtropics) and varies little on multidecadal time scales. In the western subpolar region and the subtropics, the level of no motion varies considerably on decadal and possibly longer time scales, suggesting that the barotropic component is changing, although the reason for this is as yet unclear.

Topics for future investigation include the impact of the mean North Atlantic Current, the lag between subpolar and subtropical variability, and the origin of the ageostrophic currents in the subtropical gyre.

An important follow-up would be to understand how well climate models reproduce the observed behavior. The wave propagation process encodes substantial predictability into the system and offers the possibility of understanding barriers to predictability, of discriminating between models, and is potentially a very powerful emergent constraint on climate model projections.

Finally, understanding the relationship between upper ocean heat content and sea surface temperature on decadal time scales remains an important and challenging topic. Future work should include finding methods to extend previous interannual time scale studies of the mixed layer heat budget (Buckley et al. 2014; Roberts et al. 2017; Josey and Sinha 2022) to decadal time scales.

**Acknowledgments.** This research was supported by the NERC Atlantic Climate System Integrated Study (ACSIS) Programme (NE/N018044/1); the NERC Wider Impacts of Subpolar North Atlantic decadal variability on the ocean and atmosphere (WISHBONE) project (NE/T013540/1); the NERC Climate Change in the Arctic-North Atlantic region and impacts on the U.K. (CANARI) Programme; and CLASS (NE/R015953/1) and the NERC funded RAPID AMOC programme at 26°N. This research has received funding from the European Union's Horizon 2020 research and innovation programme under Grant Agreement 820989 (COMFORT). The work reflects only the authors' view; the European Commission and their executive agency are not responsible for any use that may be made of the information the work contains. We acknowledge useful discussions with Joel Hirschi, David Smeed, Thierry Penduff, Kristofer Doos, and Florian Sévellec.

**Data availability statement.** All observational datasets used in this study are in the public domain (see references in section 2a), as is the NEMO GO6 model configuration.

## REFERENCES

- Booth, B. B. B., N. J. Dunstone, P. R. Halloran, T. Andrews, and N. Bellouin, 2012: Aerosols implicated as a prime driver of twentieth-century North Atlantic climate variability. *Nature*, **484**, 228–232, <https://doi.org/10.1038/nature10946>.
- Buckley, M. W., and J. Marshall, 2016: Observations, inferences, and mechanisms of the Atlantic meridional overturning circulation: A review. *Rev. Geophys.*, **54**, 5–63, <https://doi.org/10.1002/2015RG000493>.
- , R. M. Ponte, G. Forget, and P. Heimbach, 2014: Low-frequency SST and upper-ocean heat content variability in the North Atlantic. *J. Climate*, **27**, 4996–5018, <https://doi.org/10.1175/JCLI-D-13-00316.1>.
- Chelton, D. B., and M. G. Schlax, 1996: Global observations of oceanic Rossby waves. *Science*, **272**, 234–238, <https://doi.org/10.1126/science.272.5259.234>.
- Clement, A., K. Bellomo, L. N. Murphy, M. A. Cane, T. Mauritsen, G. Rädel, and B. Stevens, 2015: The Atlantic multidecadal

- oscillation without a role for ocean circulation. *Science*, **350**, 320–324, <https://doi.org/10.1126/science.aab3980>.
- Copernicus Climate Change Service, Climate Data Store, 2018: Sea level gridded data from satellite observations for the global ocean from 1993 to present. Copernicus Climate Change Service (C3S) Climate Data Store (CDS), accessed 10 October 2023, <https://doi.org/10.24381/cds.4c328c78>.
- Desbruyères, D. G., and Coauthors, 2020: Importance of boundary processes for heat uptake in the subpolar North Atlantic. *J. Geophys. Res. Oceans*, **125**, e2020JC016366, <https://doi.org/10.1029/2020JC016366>.
- Draws, A., and R. J. Greatbatch, 2017: Evolution of the Atlantic multidecadal variability in a model with an improved North Atlantic Current. *J. Climate*, **30**, 5491–5512, <https://doi.org/10.1175/JCLI-D-16-0790.1>.
- Emery, W. J., and R. E. Thomson, 1997: *Data Analysis Methods in Physical Oceanography*. Pergamon, 634 pp.
- Enfield, D. B., A. M. Mestas-Núñez, and P. J. Trimble, 2001: The Atlantic multidecadal oscillation and its relation to rainfall and river flows in the continental U.S. *Geophys. Res. Lett.*, **28**, 2077–2080, <https://doi.org/10.1029/2000GL012745>.
- Gastineau, G., and C. Frankignoul, 2015: Influence of the North Atlantic SST variability on the atmospheric circulation during the twentieth century. *J. Climate*, **28**, 1396–1416, <https://doi.org/10.1175/JCLI-D-14-00424.1>.
- , J. Mignot, O. Arzel, and T. Huck, 2018: North Atlantic Ocean internal decadal variability: Role of the mean state and ocean-atmosphere coupling. *J. Geophys. Res. Oceans*, **123**, 5949–5970, <https://doi.org/10.1029/2018JC014074>.
- Good, S. A., M. J. Martin, and N. A. Rayner, 2013: EN4: Quality controlled ocean temperature and salinity profiles and monthly objective analyses with uncertainty estimates. *J. Geophys. Res. Oceans*, **118**, 6704–6716, <https://doi.org/10.1002/2013JC009067>.
- Griffies, S. M., and Coauthors, 2016: OMIP contribution to CMIP6: Experimental and diagnostic protocol for the physical component of the ocean model intercomparison project. *Geosci. Model Dev.*, **9**, 3231–3296, <https://doi.org/10.5194/gmd-9-3231-2016>.
- Hersbach, H., and Coauthors, 2020: The ERA5 global reanalysis. *Quart. J. Roy. Meteor. Soc.*, **146**, 1999–2049, <https://doi.org/10.1002/qj.3803>.
- Hirshi, J. J.-M., and Coauthors, 2020: The Atlantic meridional overturning circulation in high resolution models. *J. Geophys. Res. Oceans*, **125**, e2019JC015522, <https://doi.org/10.1029/2019JC015522>.
- Hunke, E. C., and J. K. Dukowicz, 1997: An elastic–viscous–plastic model for sea ice dynamics. *J. Phys. Oceanogr.*, **27**, 1849–1867, [https://doi.org/10.1175/1520-0485\(1997\)027<1849:AEVPMF>2.0.CO;2](https://doi.org/10.1175/1520-0485(1997)027<1849:AEVPMF>2.0.CO;2).
- Josey, S. A., and B. Sinha, 2022: Subpolar Atlantic Ocean mixed layer heat content variability is increasingly driven by an active ocean. *Commun. Earth Environ.*, **3**, 111, <https://doi.org/10.1038/s43247-022-00433-6>.
- Killworth, P. D., D. B. Chelton, and R. A. de Szoeke, 1997: The speed of observed and theoretical long extratropical planetary waves. *J. Phys. Oceanogr.*, **27**, 1946–1966, [https://doi.org/10.1175/1520-0485\(1997\)027<1946:TSEOAT>2.0.CO;2](https://doi.org/10.1175/1520-0485(1997)027<1946:TSEOAT>2.0.CO;2).
- Knight, J. R., C. K. Folland, and A. A. Scaife, 2006: Climate impacts of the Atlantic multidecadal oscillation. *Geophys. Res. Lett.*, **33**, L17706, <https://doi.org/10.1029/2006GL026242>.
- Kushnir, Y., 1994: Interdecadal variations in North Atlantic sea-surface temperature and associated atmospheric conditions. *J. Climate*, **7**, 141–157, [https://doi.org/10.1175/1520-0442\(1994\)007<0141:IVINAS>2.0.CO;2](https://doi.org/10.1175/1520-0442(1994)007<0141:IVINAS>2.0.CO;2).
- Lai, W. K. M., J. I. Robson, L. J. Wilcox, and N. Dunstone, 2022: Mechanisms of internal atlantic multidecadal variability in HadGEM3-GC3.1 at two different resolutions. *J. Climate*, **35**, 1365–1383, <https://doi.org/10.1175/JCLI-D-21-0281.1>.
- Madec, G., and NEMO Team, 2016: NEMO ocean engine. Note du Pole de modelisation de l'Institut Pierre-Simon Laplace 27, ISSN No 1288-1619, 412 pp., [https://www.earth-prints.org/bitstream/2122/13309/1/NEMO\\_book.pdf](https://www.earth-prints.org/bitstream/2122/13309/1/NEMO_book.pdf).
- McCarthy, G. D., I. D. Haigh, J. J.-M. Hirshi, J. P. Grist, and D. A. Smeed, 2015: Ocean impact on decadal Atlantic climate variability revealed by sea-level observations. *Nature*, **521**, 508–510, <https://doi.org/10.1038/nature14491>.
- Menary, M. B., D. L. R. Hodson, J. I. Robson, R. T. Sutton, and R. A. Wood, 2015: A mechanism of internal decadal Atlantic Ocean variability in a high-resolution coupled climate model. *J. Climate*, **28**, 7764–7785, <https://doi.org/10.1175/JCLI-D-15-0106.1>.
- Moat, B. I., and Coauthors, 2019: Insights into decadal North Atlantic sea-surface temperature and ocean heat content variability from an eddy-permitting coupled climate model. *J. Climate*, **32**, 6137–6161, <https://doi.org/10.1175/JCLI-D-18-0709.1>.
- , B. A. King, and C. R. Macintosh, 2021: Subpolar North Atlantic ocean heat content (surface to 1000 m) using objectively mapped Argo profiling float data. NERC EDS British Oceanographic Data Centre NOC, accessed 3 December 2021, <https://doi.org/10.5285/d23c26bc-6e6c-5bbf-e053-6c86abc02cfb>.
- Msadek, R., and C. Frankignoul, 2009: Atlantic multidecadal oceanic variability and its influence on the atmosphere in a climate model. *Climate Dyn.*, **33**, 45–62, <https://doi.org/10.1007/s00382-008-0452-0>.
- Muir, L. C., and A. V. Fedorov, 2017: Evidence of the AMOC interdecadal mode related to westward propagation of temperature anomalies in CMIP5 models. *Climate Dyn.*, **48**, 1517–1535, <https://doi.org/10.1007/s00382-016-3157-9>.
- Otterå, O. H., M. Bentsen, H. Drange, and L. Suo, 2010: External forcing as a metronome for Atlantic multidecadal variability. *Nat. Geosci.*, **3**, 688–694, <https://doi.org/10.1038/ngeo955>.
- Pond, S., and G. L. Pickard, 1983: *Introductory Dynamical Oceanography*. 2nd ed. Butterworth-Heinemann, 329 pp.
- Roberts, C. D., M. D. Palmer, R. P. Allan, D. G. Desbruyères, P. Hyder, C. Liu, and D. Smith, 2017: Surface flux and ocean heat transport convergence contributions to seasonal and interannual variations of ocean heat content. *J. Geophys. Res. Oceans*, **122**, 726–744, <https://doi.org/10.1002/2016JC012278>.
- Robson, J., P. Ortega, and R. Sutton, 2016: A reversal of climatic trends in the North Atlantic since 2005. *Nat. Geosci.*, **9**, 513–517, <https://doi.org/10.1038/ngeo2727>.
- , and Coauthors, 2018: Recent multivariate changes in the North Atlantic climate system, with a focus on 2005–2016. *Int. J. Climatol.*, **38**, 5050–5076, <https://doi.org/10.1002/joc.5815>.
- , and Coauthors, 2022: The role of anthropogenic aerosol forcing in the 1850–1985 strengthening of the AMOC in CMIP6 historical simulations. *J. Climate*, **35**, 6843–6863, <https://doi.org/10.1175/JCLI-D-22-0124.1>.
- Robson, J. I., R. T. Sutton, and D. M. Smith, 2012: Initialized decadal predictions of the rapid warming of the North Atlantic Ocean in the mid 1990s. *Geophys. Res. Lett.*, **39**, L19713, <https://doi.org/10.1029/2012GL053370>.
- Sévellec, F., and A. V. Fedorov, 2013: The leading, interdecadal eigenmode of the Atlantic Meridional Overturning Circulation

- in a realistic ocean model. *J. Climate*, **26**, 2160–2183, <https://doi.org/10.1175/JCLI-D-11-00023.1>.
- , and —, 2015: Optimal excitation of AMOC decadal variability: Links to the subpolar ocean. *Prog. Oceanogr.*, **132**, 287–304, <https://doi.org/10.1016/j.pocean.2014.02.006>.
- , and T. Huck, 2015: Theoretical investigation of the Atlantic multidecadal oscillation. *J. Phys. Oceanogr.*, **45**, 2189–2208, <https://doi.org/10.1175/JPO-D-14-0094.1>.
- , and B. Sinha, 2018: Predictability of decadal Atlantic meridional overturning circulation variations. *Oxford Encyclopedia of Climate Science*, Oxford University Press, 44 pp., <https://doi.org/10.1093/acrefore/9780190228620.013.81>.
- Smith, D. M., and J. M. Murphy, 2007: An objective ocean temperature and salinity analysis using covariances from a global climate model. *J. Geophys. Res.*, **112**, C02022, <https://doi.org/10.1029/2005JC003172>.
- , and Coauthors, 2015: Earth's energy imbalance since 1960 in observations and CMIP5 models. *Geophys. Res. Lett.*, **42**, 1205–1213, <https://doi.org/10.1002/2014GL062669>.
- Storkey, D., and Coauthors, 2018: UK global ocean GO6 and GO7: A traceable hierarchy of model resolutions. *Geosci. Model Dev.*, **11**, 3187–3213, <https://doi.org/10.5194/gmd-11-3187-2018>.
- Stramma, L., 1984: Geostrophic transport in the warm water sphere of the eastern subtropical North Atlantic. *J. Mar. Res.*, **42**, 537–558, <https://doi.org/10.1357/002224084788506022>.
- Sutton, R. T., and B. Dong, 2012: Atlantic Ocean influence on a shift in European climate in the 1990s. *Nat. Geosci.*, **5**, 788–792, <https://doi.org/10.1038/ngeo1595>.
- , G. D. McCarthy, J. Robson, B. Sinha, A. T. Archibald, and L. J. Gray, 2018: Atlantic multidecadal variability and the U.K. ACSIS program. *Bull. Amer. Meteor. Soc.*, **99**, 415–425, <https://doi.org/10.1175/BAMS-D-16-0266.1>.
- Swingedouw, D., P. Ortega, J. Mignot, E. Guilyardi, V. Masson-Delmotte, P. G. Butler, M. Khodri, and R. Séférian, 2015: Bidecadal North Atlantic ocean circulation variability controlled by timing of volcanic eruptions. *Nat. Commun.*, **6**, 6545, <https://doi.org/10.1038/ncomms7545>.
- Tsujino, H., and Coauthors, 2020: Evaluation of global ocean–sea-ice model simulations based on the experimental protocols of the Ocean Model Intercomparison Project Phase 2 (OMIP-2). *Geosci. Model Dev.*, **13**, 3643–3708, <https://doi.org/10.5194/gmd-13-3643-2020>.
- Wang, H., Z. Li, X. Lin, J. Zhao, and D. Wu, 2022: Adiabatic processes contribute to the rapid warming of subpolar North Atlantic during 1993–2010. *J. Geophys. Res. Oceans*, **127**, e2021JC018234, <https://doi.org/10.1029/2021JC018234>.
- WCRP, 2023a: Explaining and predicting Earth system change. <https://www.wcrp-climate.org/epesc>.
- , 2023b: Grand challenge on near-term climate prediction. <https://www.wcrp-climate.org/gc-near-term-climate-prediction>.
- Yeager, S. G., and J. I. Robson, 2017: Recent progress in understanding and predicting Atlantic decadal climate variability. *Curr. Climate Change Rep.*, **3**, 112–127, <https://doi.org/10.1007/s40641-017-0064-z>.
- Zhang, J., and R. Zhang, 2015: On the evolution of Atlantic meridional overturning circulation fingerprint and implications for decadal predictability in the North Atlantic. *Geophys. Res. Lett.*, **42**, 5419–5426, <https://doi.org/10.1002/2015GL064596>.
- Zhang, R., 2008: Coherent surface-subsurface fingerprint of the Atlantic Meridional Overturning Circulation. *Geophys. Res. Lett.*, **35**, L20705, <https://doi.org/10.1029/2008GL035463>.
- , R. Sutton, G. Danabasoglu, Y.-O. Kwon, R. Marsh, S. G. Yeager, D. E. Amrhein, and C. M. Little, 2019: A review of the role of the Atlantic Meridional Overturning Circulation in Atlantic multidecadal variability and associated climate impacts. *Rev. Geophys.*, **57**, 316–375, <https://doi.org/10.1029/2019RG000644>.